Shedding light on reovirus assembly—Multimodal imaging of viral factories

Eva Durinova[a,b], Peter Mojzes[c], Tomas Bily[a,b], Zdenek Franta[a], Tomas Fessl[a], Alexander Borodavka[d], and Roman Tuma[a,*]

[a]Faculty of Science, University of South Bohemia, Ceske Budejovice, Czech Republic
[b]Biology Centre, Czech Academy of Sciences, Ceske Budejovice, Czech Republic
[c]Faculty of Mathematics and Physics, Charles University, Prague, Czech Republic
[d]Department of Biochemistry, University of Cambridge, Cambridge, United Kingdom
*Corresponding author. e-mail address: rtuma@prf.jcu.cz

Contents

Abstract

Avian (ortho)reovirus (ARV), which belongs to *Reoviridae* family, is a major domestic fowl pathogen and is the causative agent of viral tenosynovitis and chronic respiratory disease in chicken. ARV replicates within cytoplasmic inclusions, so-called viral factories, that form by phase separation and thus belong to a wider class of biological condensates. Here, we evaluate different optical imaging methods that have been developed or adapted to follow formation, fluidity and composition of viral factories and compare them with the complementary structural information obtained by well-established transmission electron microscopy and electron tomography. The molecular and cellular biology aspects for setting up and following virus infection in cells by imaging are described first. We then demonstrate that a wide-field version of fluorescence recovery after photobleaching is an effective tool to measure fluidity of mobile viral factories.

Advances in Virus Research
ISSN 0065-3527
https://doi.org/10.1016/bs.aivir.2023.06.002

A new technique, holotomographic phase microscopy, is then used for imaging of viral factory formation in live cells in three dimensions. Confocal Raman microscopy of infected cells provides "chemical" contrast for label-free segmentation of images and addresses important questions about biomolecular concentrations within viral factories and other biological condensates. Optical imaging is complemented by electron microscopy and tomography which supply higher resolution structural detail, including visualization of individual virions within the three-dimensional cellular context.

1. Introduction

Viruses as intracellular parasites are subverting cell structure for replication and assembly. While viral protein production is hijacking and reprogramming cellular ribosomes, genome replication and transcription require virus-encoded enzymes, e.g., polymerases, helicases, capping enzymes, and other accessory proteins. These accessory proteins are commonly called "non-structural" since they are not part of the mature virion, however they provide the structural framework for assembly of replication complexes (and often possess well defined three-dimensional structures). Many simple RNA viruses remodel cellular membranes to assemble their membrane bound replication complexes (Kopek et al., 2007). Due to their attachment to prominent cellular structures, such as endoplasmic reticulum (ER), these complexes appear quasistatic at intermediate resolution and can be conveniently studied by light, electron microscopy (EM) (Sachse et al., 2019) and electron tomography (ET) (de Castro et al., 2021) using fixed samples.

On the other hand, more complex dsRNA viruses replicate in cytoplasmic inclusions which are called viral inclusion bodies or viral factories (VF) that appear mobile and most likely form by liquid-liquid phase separation (LLPS) (Hyman et al., 2014; Zwicker et al., 2014) as recently shown for rotavirus (Geiger et al., 2021; Papa et al., 2021). Such dynamic structures, which belong to a broader class of biological condensates, exhibit droplet-like behavior including mobility, fission and fusion and change shape to flow around more static intracellular obstacles. Such objects need to be studied by combination of time-resolved microscopies that provide information about the dynamic parameters of the droplets, such as internal viscosity, mass exchange with the surrounding cytoplasm and local mobility. With the advent of genetically encoded fluorescence protein tags, live cell imaging by fluorescence microscopy became mainstream and allows to study dynamic events such as VF droplet fusion and fission. A variant of fluorescence imaging which is called fluorescence recovery after photobleaching

has been previously developed to estimate fluidity of biological membranes and measure diffusion within cells (Axelrod et al., 1976). This tool quickly became indispensable in the study of biological condensates and is used to demonstrate internal fluidity as well as mass exchange across the boundary (Taylor et al., 2019).

One of the defining features of biological condensates is the higher internal concentration of selected components, e.g., specific proteins and/or nucleic acids. This is expected to be accompanied by the exclusion of cytoplasmic proteins from such condensates, although it is difficult to quantitatively estimate the exact composition of condensates in situ within cells. In principle, an emerging field of imaging mass spectrometry (MS) and quantitative proteomics can be useful for such estimates. However, currently, these techniques are limited to small molecules (Zhu et al., 2021) or only useful for isotopic composition analysis (Pasulka et al., 2018) due to difficulties associated with desorption and fragmentation of large macromolecules within cells. Confocal Raman microscopy (CRM) emerged as a tool to study subcellular distribution and concentration of biomolecules (Mojzes et al., 2020; Moudrikova et al., 2021), including virus infected cells (Yakubovskaya et al., 2021). Raman spectroscopy (RS) has been used to study virus assembly in vitro for many years (Nemecek et al., 2013; Tuma et al., 1998; Tuma and Thomas, 1997), hence there is a wealth of information (Tuma, 2005) ready to assist the interpretation of spatially resolved spectral signatures. Another CRM advantage is the possibility of label free imaging, a feature particularly important for studying biological condensates, since even small modifications (e.g., hexahistidine or fluorescent tags) may perturb or abrogate phase separation and impacting its biological function.

Due to the intrinsically low Raman signal CRM requires slow scanning during confocal imaging and thus is usually applied to fixed cells. A faster label-free alternative have emerged in the form of phase holotomographic microscopy (Cotte et al., 2013) that has been recently commercialized (3D cell explorer by Nanolive https://www.nanolive.ch/). This technology images refractive index in three dimensions (3D) with a spatial resolution comparable to a typical confocal microscope with a rapid frame rate (2 fps for high resolution 3D cube $90 \times 90 \times 45$ μm). Given that the refractive index is proportional to biomolecular density (concentration) this methodology can be, in principle, suitable for imaging the dense viral condensates in real time, allowing to differentiate them from, e.g., less dense vesicles, lipid droplets or other inclusions (Sandoz et al., 2019).

Fluorescent imaging has been used to study mammalian reovirus in cell culture (Miller et al., 2003) as well as in a whole organism (oncolytic MRV T1L (Kanai et al., 2019). The cell entry pathway of *Scophthalmus maximus* reovirus (SMReV, aquareovirus, turbot host) was imaged in real time using tracking of individual viral particles that were tagged with quantum dots (Liu et al., 2018). The 3D confocal imaging was subsequently complemented by electron microscopy on thin cell sections. In this review, we focus on imaging VF formation and avian reovirus assembly in cells, and evaluate the merits of both established (FRAP, thin section EM and serial electron tomography, ET) and emerging techniques, e.g., holotomographic microscopy (HTM) and confocal Raman microscopy (CRM).

2. *Reoviridae* and avian reovirus

Avian (ortho)reovirus (ARV) belongs to the large family of *Reoviridae*, which has a wide host range from fungi to vertebrates (Knipe and Howley, 2013). *Reoviridae* include serious human pathogens such as rotaviruses (RV) causing life-threatening diarrheal diseases in infants and young children, important plant pathogens, such as the rice dwarf virus, and viruses causing important livestock and poultry diseases (e.g. bluetongue virus (BTV) (Roy, 2020) and ARV (Benavente and Martinez-Costas, 2007)). ARV inflicts significant economic loses to worldwide poultry industry mainly by causing viral arthritis (tenosynovitis) and chronic respiratory disease in chicken (Walker et al., 1972).

The ARV genome has 10 linear segments packed inside a double-layered icosahedral protein shell (outer capsid has 85 nm in diameter, Fig. 1A) (Zhang et al., 2005). The capsid lacks a lipid envelope, which is a common feature of the *Reoviridae* family. The inner capsid is transcriptionally active and remains intact during replication producing mRNA molecules as well as copies of the dsRNA segments (Benavente and Martinez-Costas, 2007). ARV genomic segments are divided into three groups (large L, medium M, small S) with corresponding proteins designated by Greek letters λ, μ and σ, respectively, followed by a letter (e.g., λA, λB etc., note the difference from the mammalian reovirus, MRV, which uses numbers). The genome codes at least twelve primary translation products, 8 structural (part of the virion) and 4 non-structural (NS) proteins. The latter NS proteins do not contribute to the virion structure but they are essential for replication, gene packaging and virion assembly.

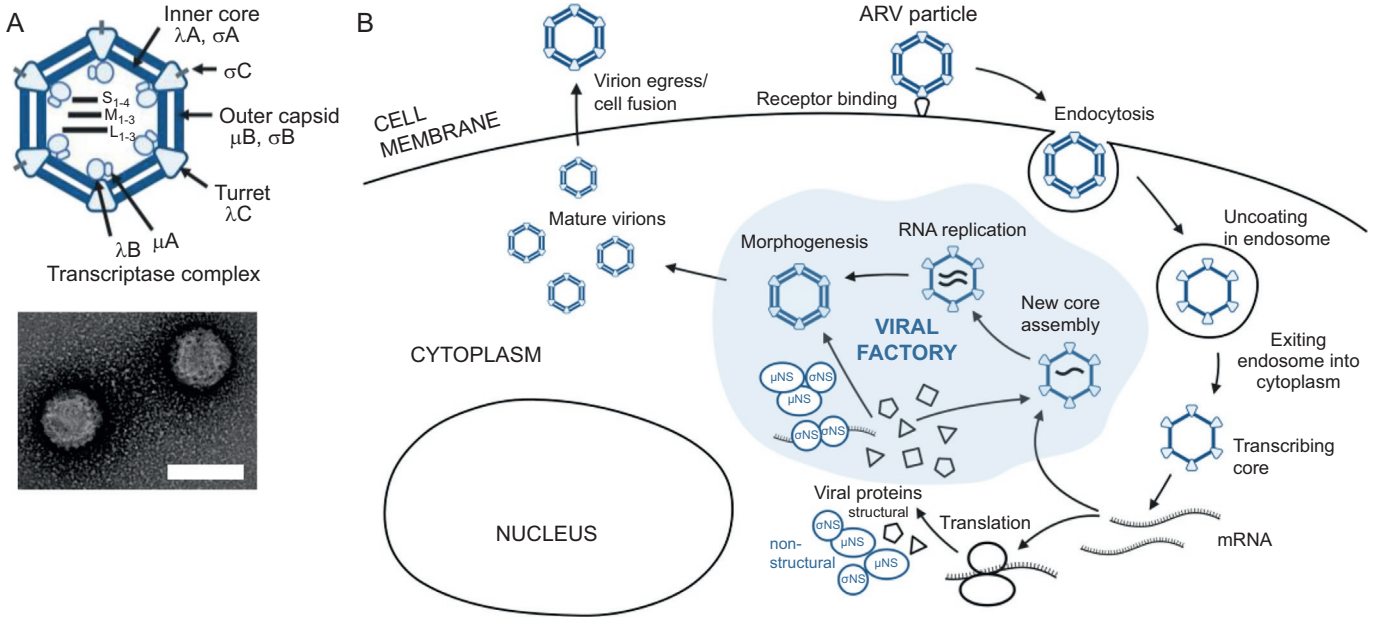

Fig. 1 ARV structure and assembly. (A) Top: Schematics of ARV virion structure with proposed location of key structural proteins indicated by arrows. Bottom panel shows negatively stained transmission EM of purified virions. ARV (vaccine strain 1133, Nobilis Reo 1133) was amplified in BHK-21 (Baby Hamster Kidney) cell line which was used in this work for all imaging purposes instead of the typical host cells (chicken embryonic fibroblasts) which are used for large scale production. The virus was purified from the lysate by differential and CsCl density gradient centrifugation (Grande and Benavente, 2000). The particles were adhered to carbon coated copper grids, stained with 1.2% uranyl acetate, and visualized in Jeol 1400Flash 120 kV electron microscope. (B) Simplified schematics of ARV infection cycle. Based on (Benavente and Martinez-Costas, 2007). Created with BioRender.com.

ARV enters cells by receptor mediated endocytosis (Martinez-Costas et al., 1997) and infection starts when the transcriptionally active cores get liberated from the endosomes and start producing mRNA which is then translated by the host ribosome (Fig. 1B) (Benavente and Martinez-Costas, 2007). The replication cycle of ARV takes place within the cytoplasm, in the so-called viral factories (VF) (Benavente and Martinez-Costas, 2007). VF are dense inclusion bodies (neoorganelles) formed within hours post infection by self-assembly (or condensation) of the two most abundant NS proteins, μNS and σNS. The former, μNS, recruits σNS and other viral proteins (Touris-Otero et al., 2004) while the latter acts as an RNA chaperone in genome assortment and packaging (Borodavka et al., 2015; Bravo et al., 2018; Strauss et al., 2023).

Cytoplasmic viral factories are a shared characteristic of *Reoviridae* but they differ in their morphology, self-assembly and genome segment assortment mechanisms (Borodavka et al., 2018). For example, overexpression of two rotavirus non-structural proteins, NSP2 and NSP5, is necessary and sufficient for formation of VF like structures in cells and in vitro (Papa et al., 2021) while overexpression of ARV μNS alone is sufficient for VF-like inclusions to appear in cells (Touris-Otero et al., 2004). MRV also assembles in neoorganelles (Tenorio et al., 2019) and σNS has been implicated in RNA recruitment into VF (Lee et al., 2021). Recent studies of RV factories demonstrated that they form by LLPS which is primarily driven by protein-protein interactions (Geiger et al., 2021; Nichols et al., 2023). RNA-protein interactions were implicated in the fluidity and formation of blue tongue virus VFs (Rahman et al., 2022). Based on the similar VF appearance the liquid-like VF behavior could be universal among *Reoviridae* but their cell localization and trafficking is likely to differ (Broering et al., 2002; de Castro et al., 2021; Fernandez de Castro et al., 2014; Lee et al., 2021; Tenorio et al., 2018, 2019). Below, we describe the necessary methodology and demonstrate its use to establish liquid-like behavior of ARV factories.

Given the dense and potentially liquid-like character of VFs little is known about virion assembly and genome packaging inside these condensates. It has emerged for RV and BTV that genome packaging and assortment is mediated by RNA-RNA interactions between single-stranded segment precursors (Papa et al., 2021; Strauss et al., 2023; Sung et al., 2019) that are, in the RV case, mediated by NSP2 (Bravo et al., 2021). Given the mechanistic similarities between RV NSP2 and ARV σNS (Bravo et al., 2018, 2021) it is likely that the same RNA-driven assortment mechanism also applies to reovirus genome assembly.

Reoviruses generally use a variety of virion egress routes (Labadie et al., 2020; Roth et al., 2021). ARV, unlike MRV, is a fusogenic virus, i.e., its replication results in cell fusion at later stages of infection, producing multinucleated syncytia (Bodelon et al., 2002). This mechanism promotes cell-to-cell virus spreading between cells within tissues or a cell culture. The resulting syncytia are thus a good marker of viral infection in cell culture.

Taken together, *Reoviridae* VFs are likely formed by LLPS. Hence, we focus this review on imaging techniques that are suitable for characterization of such liquid condensates such as FRAP. In addition, live cell 3D HTM imaging shall be able to address spatial and temporal organization of VFs inside cells, in a fashion like the recent comprehensive MRV study (Kniert et al., 2022). CRM aims to delineate the associated changes in VF density and composition (e.g., RNA, protein, lipid) throughout the infection. These techniques are selected to complement the wealth of fluorescence and EM imaging of MRV assembly (de Castro et al., 2021; Desmet et al., 2014; Diestra et al., 2009; Kaufer et al., 2012; Lee et al., 2021; Sachse et al., 2019; Tenorio et al., 2018, 2019).

3. Fluorescent imaging of viral factories

3.1 Preparation of stable cell lines expressing fluorescently tagged NS proteins

To be able to follow VF formation and dynamics we needed to introduce fluorescently tagged proteins that would partition into the neoorganelles. One strategy, which has been successfully used to study RV replication (Geiger et al., 2021), is engineering NS proteins terminally tagged with a fluorescent protein. Transient transfection prior to each infection is laborious and often leads to variable levels of expression in individual cells. This may pose problems if the tagged NS version has different phase separation properties that may disrupt VF formation. Hence, generation of stable cell lines with low, but detectable levels of fluorescently tagged NS expression is generally preferred. The cell line needs to be permissible to viral replication and suitable to the selected range of intended imaging techniques. The RV system employs a stable cell line MA104 that expresses NSP5-eGFP. This cell line was used to demonstrate VF fluidity (Geiger et al., 2021), and to localize viral transcripts in viroplasms by single molecule FISH (Strauss et al., 2023). Here we used the RV-MA104-NSP5 system to develop Raman spectral imaging for label-free VF localization. We developed a similar system to follow ARV infection in BHK-21 stable cell line as

described in the following section. We selected mammalian BHK-21 (baby hamster kidney) cells that are susceptible to ARV infection by the ARV strain S1133 (Simoni et al., 1999), and are suitable for live cell imaging. We describe generation of BHK-21 cell lines stably expressing low levels of C-terminally tagged μNS-mCherry and σNS-mCherry fusions, respectively. We had also prepared cell lines with eGFP fusions, but these proved unsuitable for multimodal imaging due to high autofluorescence interfering in the green spectral region.

3.1.1 Preparation of σNS and μNS-mCherry fusion constructs

Fusion constructs linking mCherry fluorescence protein to the C terminus of either σNS or μNS via a short flexible linker (GSA GSA AGS GEF) (Waldo et al., 1999) were designed using NEBuilder® online assembly tool (NEB). Genes encoding σNS and μNS were derived from the Avian orthoreovirus strain 1733 (without the stop codon) and amplified using σNS-F, R and μNS-F, R primers, respectively (Table 1). The gene encoding mCherry (without its start codon) was amplified either using mCherrS-F or mCherrU-F, and mCherry-R primers. The σNS-R, μNS-R and mCherrS-F, mCherrU-F primers included the sequence for flexible linker. Amplified σNS, μNS and both mCherry fragments were assembled into pUC19 cloning vector (amplified using pUC19F, R primers) via the NEBuilder® HiFi DNA Assembly Master Mix (NEB) and sequence verified. Resulting fusion genes were reamplified (σNS-C-Attb-F or μNS-C-Attb-F, and mCherry-C-Attb-R primers, Table 1), purified and inserted into the pDONR207 vector by Gateway® BP (Invitrogen). The resulting sequence verified donor constructs were inserted into the pcDNA3.1/nV5-DEST destination vector by Gateway LR recombination reaction. Resulting σNS-C-mCherry and μNS-C-mCherry fusion constructs were purified by NucleoBond Xtra maxi kit (Macherey Nagel), linearized with *Age*I restriction enzyme (NEB) and ethanol precipitated prior to cell transfection.

3.1.2 Stable cell line generation and imaging

BHK-21 cells were grown in DMEM high glucose medium (Biosera) supplemented with 10% fetal bovine serum (Biosera) and 1% penicillin/streptomycin (Biosera) (DMEM-complete) in capped T25 cell culture flasks (TPP) at 37.5 °C with 5% CO_2. For transfection experiments, Lipofectamine™ 2000 transfection reagent (Invitrogen) was used according to the manufacturer's instructions. We seeded 1×10^6 cells (live cell count to

Table 1 Specific primers for generation of σNS-Cflex-mCherry and μNS-Cflex-mCherry constructs.

sNS-F	aaaacgacggccagtgaattcgagcATGGACAACACCGTGCGTGT[a]
sNS-R	gaattcgccagaaccagcagcggagccagcggaaccCGCCATCCTA GCTGGAGAGAC
uNS-F	aaaacgacggccagtgaattcgagcATGGCGTCAACCAAGTGGGG
uNS-R	gaattcgccagaaccagcagcggagccagcggaaccCAGATCATCCA CCAATTCTTCCATAGATG
mCherrS-F	agctaggatggcgggttccgctggctccgctgctggttctggcgaattcGTGAG CAAGGGCGAGGAGGA[b]
mCherrU-F	ggtggatgatctgggttccgctggctccgctgctggttctggcgaattcGTGAG CAAGGGCGAGGAGGA
mCherry-R	actctagaggatccccgggtaccgaCTACTTGTACAGCTCGT CCATGC
sNS-C-Attb-F	ggggacaagtttgtacaaaaaagcaggcttcgaaggagatagaaccATGGAC AACACCGTGCGTGTTG
uNS-C-Attb-F	ggggacaagtttgtacaaaaaagcaggcttcgaaggagatagaaccATGGC GTCAACCAAGTGGGGAG
mCherry-C-Attb-R	ggggaccactttgtacaagaaagctgggttTTACTTGTACAGCTC GTCCATGC
pUC19-F	TCGGTACCCGGGGATCCTCT
pUC19-R	GCTCGAATTCACTGGCCGTC

[a]amplicon specific parts are in capitals.
[b]Fusion linker (GSA GSA AGF GEF) underlined.

be 60–80% confluent at day of transfection) into T25 cell culture flasks (TPP) in 10 mL of DMEM-complete and allowed them to settle for 24 h. Prior the transfection, DMEM-complete was replaced by 4 mL of DMEM without FBS and 1% penicillin/streptomycin. Next 10 μg of linearized plasmid DNA was added into 500 μL of Opti-MEM® Reduced Serum Medium (Gibco), mixed with 500 μL of Opti-MEM® containing 15 μL of Lipofectamine™ 2000 and incubated at room temperature for 10 min. Resulting DNA complexes were added dropwise and the BHK-21 cells were transfected for 24 h at 37.5 °C with 5% CO_2. The transfection medium was then replaced with 10 mL of fresh DMEM

supplemented with 10% FBS and 300 μg/mL of selective antibiotic G-418 (CarlRoth). The BHK-21 cells were incubated at 37.5 °C with 5% CO_2, the medium was replaced three times a week and the cytotoxicity was monitored daily. Upon selection, the BHK-21 cells were further cultivated and frozen as a polyclonal cell line.

The outcome of transfection was monitored by live cell imaging (Fig. 2). The cultures were seeded 3×10^5 BHK-21 cells into 35-mm glass-bottomed cell culture μ-dishes (Ibidi) in 1 mL of transparent FluoroBrite DMEM (Gibco) supplemented with 10% FBS and 300 μg/mL of G-418. Cells were imaged by 3D cell explorer (Nanolive, see section **Holotomographic phase microscopy** below for details). The infected cell culture was then put to the live-cell imaging heated chamber (37 °C and 5% CO_2). As expected based on previous studies (Brandariz-Nunez et al., 2010a,b; Touris-Otero et al., 2004) μNS-C-mCherry can form VF-like globular structures even in the absence of viral infection (Fig. 2A). However, live cell imaging (Fig. 2A and Supplementary Video 1 in the online version at https://doi.org/10.1016/bs.aivir.2023.06.002) revealed considerable mobility and liquid like behavior (fission and fusion) of the μNS-C-mCherry labeled globules.

The formation of VF-like structures in the absence of viral replication makes it hard to distinguish genuine VFs in infected cells from those formed spontaneously. To monitor infection-driven VF formation we prepared the σNS-C-mCherry construct and corresponding stable cell line. The uninfected cells exhibit diffuse σNS-C-mCherry distribution (Fig. 2B left) as expected since σNS requires μNS for VF localization. The expected σNS-C-mCherry localization (into globular VFs) starts to appear at about 9 h.p.i. while almost all fluorescence signal is concentrated in VFs in later stages of infection when the cells appear as multinucleated syncytia (Fig. 2B right). Note that since only few cells within the field of view express σNS-C-mCherry and VF formation can happen within a wide period post infection it is almost impossible to "catch" the onset of VF formation in real time with this experimental setup (HTM fluorescence). Another limitation is considerable photobleaching during time lapse video due to optical path limitations and limited fluorescence detector within the commercial HTM setup. However, 3D refractive index imaging provides information about the cellular context and its remodeling during infection as manifested by the drastically changed, multinuclear appearance of the syncytium in Fig. 2B (right). Low excitation dose fluorescent imaging, such as wide-field FRAP that is described in the next chapter, provides complementary view of faster VF dynamics.

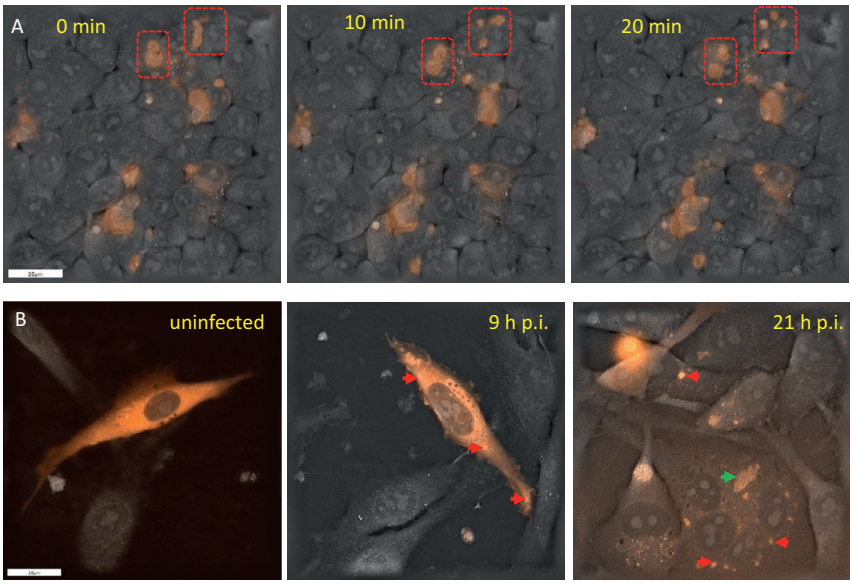

Fig. 2 Imaging of BHK-21 stable cell line expressing tagged NS proteins using fluorescence and HTM. (A) Time lapse of area containing confluent cells expressing μNS-C-mCherry fusion (times indicated in individual panels). Regions of interest exhibiting droplet-like behavior are designated by red dashed boxes. See also accompanying video (Supplementary Video 1 in the online version at https://doi.org/10.1016/bs.aivir.2023.06.002). (B) Imaging cells expressing σNS-C-mCherry fusion. Uninfected cells (left) and cells (different fields of view) post infection (hour post infection indicated) with ARV strain S1133 (multiplicity of infection 10) are shown. Globular VFs are indicated by red arrows while the late pleiomorphic VF is labeled by green arrow (right panel). Scale bar 20 μm. Images represent overlays of refractive index focal slice (grayscale) with mCherry fluorescence (orange).

3.2 Fluorescence recovery after photobleaching

FRAP is a well-established method for study of biomolecular diffusive motion within cellular context {Axelrod, 1976 #164}. The principle is schematically shown in Fig. 3A. A selected spot in the cell, which expresses the fluorescently labeled diffusion probe, is exposed to a short (10 of millisecond), intense and tightly focused excitation beam (with wavelength within the fluorophore absorption). This causes photobleaching, i.e., irreversible destruction of the fluorophore, within the area. Provided there is a pool of diffusible probes within the cell then fluorescence recovery is observed. The exact recovery kinetics depends on various factors such as the bleached volume shape and dimensions, target diffusion coefficient

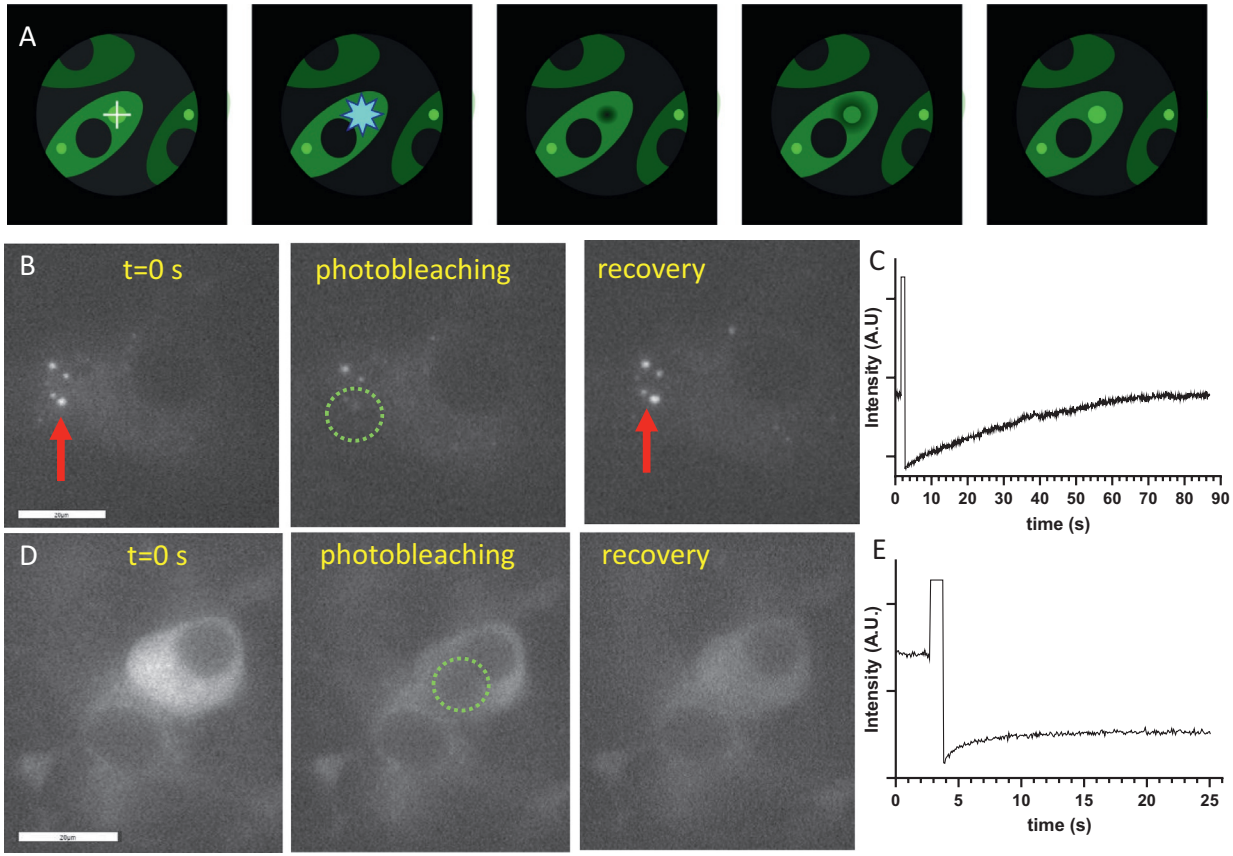

Fig. 3 See figure legend on opposite page.

and boundary permeability (Taylor et al., 2019). Usually, the bleaching and subsequent imaging is performed with a confocal microscope. Such setup offers advantage of a well-defined bleached and observation volume (3D Gaussian for a focused laser beam) that allows for quantitative interpretation of the recovery kinetics in terms of defined boundary conditions and diffusion coefficient (Taylor et al., 2019). However, fixed confocal volume monitoring is not suitable for moving objects such as VF-like droplets (Fig. 2A). Thus, we had to resort to a bespoke combination of confocal and wide field excitation with a rapid, camera-based image collection (10 ms frame resolution).

The set-up is built around Olympus IX70 inverted microscope with 60× Olympus objective (NA = 1.49, oil, APO N) an environmental stage (OKOLAB) for temperature, humidity, and CO_2 control. The excitation is provided by Toptica Chrome iCLE laser CW engine (Toptica, lines 405, 488, 561, 640 nm, with an output power up to 20 mW per line). The key modification is splitting of the excitation light into confocal bleaching and wide-field monitoring beams via a polarizing beam splitter (Thorlabs CCM1-PBS251/M). This allows the intensity of each beam to be pre-set mechanically by rotation of a half-wave plate (Thorlabs) for each set of experiments. Rapid (ms) switching between bleaching and monitoring is controlled electronically by liquid-crystal shutters (Thorlabs LCC1620/M) and synchronization with data collection is achieved via TTL pulses sent by Arduino. Wide-field illumination is generated by a passage through an extra lens which focuses the beam at the back focal plane of the objective.

Fig. 3 Fluorescence recovery after photobleaching (A) FRAP schematics: field of view is gray, fluorescent target inside cell is green (brighter spots representing VFs) and photobleaching beam is cyan (second panel). Recovery proceeds from left to right. (B) Fluorescence images of BHK-21 cell expressing σNS-C-mCherry and infected with ARV strain S1133, 9 h.p.i. Initial fluorescence prior to bleaching (left panel, tracked VF indicated with red arrow), just after bleaching (bleached spot circled green) and after recovery (80s post bleaching). (C) Fluorescence intensity of tracked VF over observation time. A large intensity spike indicates the bleaching pulse. The intensities were extracted from regions of interest in the image series using ImageJ (Rueden et al., 2017). (D) Fluorescence images of uninfected BHK-21 cells expressing σNS-C-mCherry. (E) Fluorescence intensity of the bleached cytoplasmic area (green circle) over observation time. Note that fluorescence recovery does not reach the pre-bleaching levels but instead the level of surrounding cytoplasm that became depleted due to bleaching and low level of σNS-C-mCherry expression.

The two beams are combined after this lens using a second polarizing beam splitter. The emission is separated from excitation by beam splitting mirror (Chroma, ZT405/488/561/640rpcv2) and remaining bleaching light is further reduced by a notch filter (Semrock, NF03-405/488/561/635E-25) placed directly in front of the EM-CCD camera (Ixon Ultra 897 by Andor). This double filter setup allows triggering the bleaching beam without the need for slow shutter closure, e.g., when a moving target passes through the focal point.

The main advantage of the setup is a possibility to follow recovery of multiple moving objects on millisecond to minute time scale (Fig. 3B) with quantitative estimation of recovery degree (from the pre-bleach frames and recovery plateau, Fig. 3C). There are also several drawbacks, one being the limited field of view due to the illumination geometry and beam size. In addition, wide field imaging only yields a 2D projection onto camera plane and thus the observation volume is not defined well enough for quantitative analyses (Taylor et al., 2019). However, simple analysis, which is based on direct comparison of fluorescence recovery of σNS-C-mCherry within VFs in infected cells (Fig. 3BC) with that of cytoplasmic σNS-C-mCherry in uninfected control cells (Fig. 3DE) provides enough information to reach following conclusions: i) Complete recovery of VF fluorescence within 80 s (Fig. 3C) offers convincing evidence of VF fluidity; ii) VF recovery is much slower than that of cytoplasmic σNS-C-mCherry control (bleached spot reaches equilibrium with the surrounding cytoplasm within 5 s, Fig. 3DE) suggesting higher intrinsic viscosity of VFs.

FRAP can in principle differentiate phase behavior of different VF objects, such as those identified in the right panel of Fig. 2B, based on their diffusion coefficients. This quantitative analysis will require selection of appropriate diffusion model and making assumptions about the bleached volume geometry and boundary conditions (Taylor et al., 2019). The applicability of the selected model will need to be validated, e.g., by comparison of the FRAP estimate of diffusion coefficient with that obtained by a complementary techniques, such as fluorescent correlation spectroscopy (Wei et al., 2017).

4. Holotomographic phase microscopy

Live cell imaging represents an essential tool to track progress of infection and formation of VFs inside cells. As shown in the case of MRV morphogenesis and egress it is important to localize virus assembly

within the three-dimensional cellular context and be able to follow remodeling of cellular structures such as ER and Golgi (Tenorio et al., 2018). Labeling with multiple fluorescent proteins and dyes is necessary for selective contrast but poses problems in live cells due to uneven expression and photoinduced cytotoxicity over long observation periods, especially when scanning in 3D. Advances in fast frame cameras and fast digital image processing led to the development of robust 3D holographic techniques, collectively known as holotomographic microscopy (HTM) which generate contrast from subtle changes in refractive index that are detected through optical phase changes and exploit illumination from multiple directions (Choi et al., 2007; Cotte et al., 2013).

Recently, HTM imaging has been implemented, together with wide-field fluorescence, in a commercial setup 3D Cell Explorer-fluo by Nanolive (www.nanolive.ch) (Moreno et al., 2021). Here we illustrate the use of this platform to track ARV infection and VF formation. Cell organelles or structures of interest can be identified and localized through the fluorescence and then studied non-invasively and marker-free in volume which provides the relevant cellular context. The 3D image is generated based on mapping refractive index (RI) in the volume sample (interference contrast). The volume mapping is obtained holographically using trans-illumination via rotational mirror (Fig. 4A) and light collection through a 60× objective (NA = 0.8) on a CMOS Sony IMX174 sensor (www.nanolive.ch). The volume is composed of image stacks covering the depth of 30 μm (field of view 90 × 90 μm, resolution up to 200 nm lateral and 400 nm in depth) and can be acquired every 2 s. Low phototoxicity during imaging is achieved by employing a low powered green laser ($\lambda = 520$ nm, sample exposure 0.2 mW/mm^2). In addition, up to four fluorescence detection channels are provided by a CoolLed module (for DAPI, FITC and TRITC dyes in our setup).

After infection of BHK-21 cells with S1133 ARV strain we used fluorescence to find regions with cells expressing σNS-C-mCherry at levels well above the background, i.e., suitable for long-term observation and localization of VFs (see examples in Fig. 2B). This step is essential when using polyclonal cell line which inevitably exhibits cell-to-cell variation in expression levels. Focused fluorescent image is then used to set the mid plane of the RI stack. Lower energy emission (e.g., mCherry vs eGFP tag) proved to be preferable for detecting onset of viroplasms due to autofluorescence and a higher background related to the emission channel sharing spectral bandwidth with the 532 nm transillumination holographic beam.

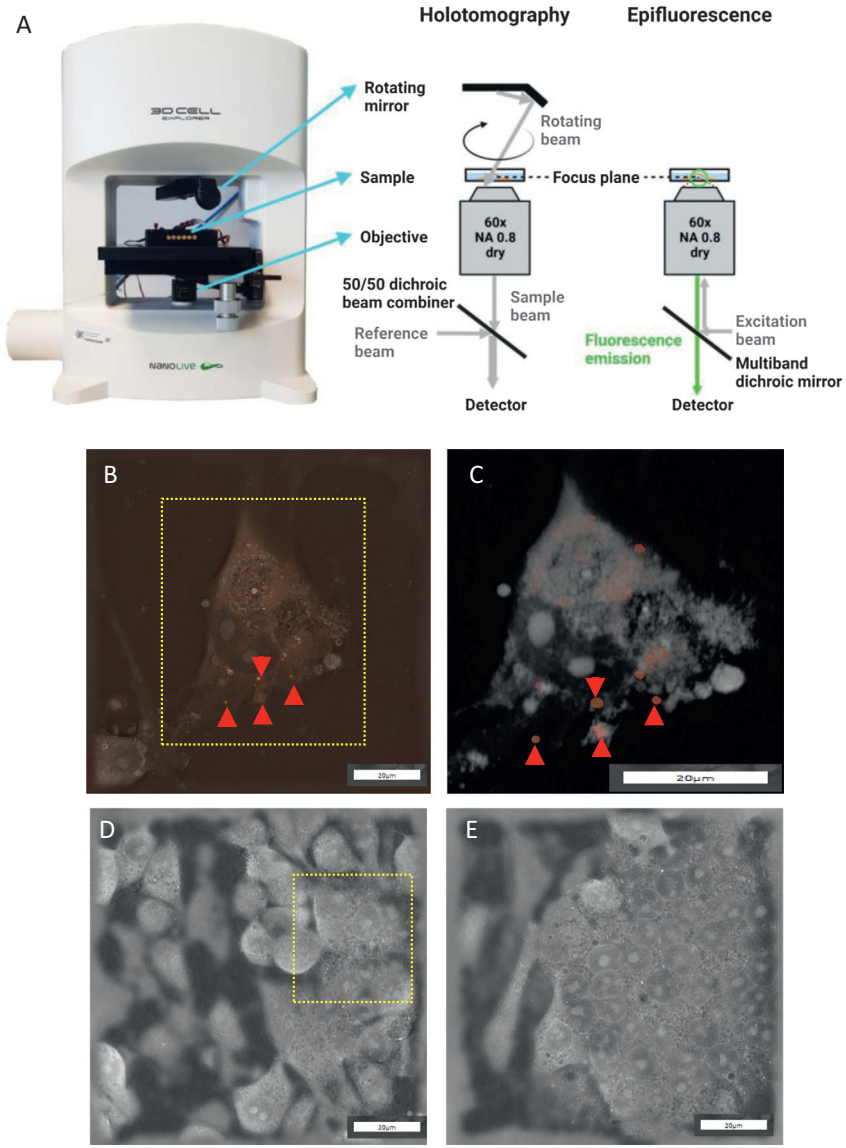

Fig. 4 Holotomographic microscopy. (A) A photograph of 3D Cell Explorer Fluor (Nanolive) setup equipped with an environmental stage (OKOLAB) (left) and a simplified scheme of HTM optical path (middle) and epifluorescence (right, Created with BioRender.com). (B) BHK-21 cells 19 h.p.i. with focused fluorescence overlayed over central RI slice. Few round VFs (identified by σNS-C-mCherry fluorescence) are marked with red arrows. (C) The area inside the yellow dotted rectangle in panel B was rendered in 3D RI densities and combined with central fluorescence slice and tilted around horizontal axis. The same spherical VFs marked by arrows as in panel B. 3D rendering done with UCSF Chimera https://www.rbvi.ucsf.edu/chimera (Goddard et al., 2018). (D) RI slice rendering of ARV infected cells 21 h.p.i. Yellow dotted box contains area with multinucleated syncytium. (E) The same area as in panel D but after an additional 7 h. See the accompanying video which illustrates the progress of infection over 7 h, one 3D frame taken every 2 min and played back at 10 fps (Supplementary Video 2 in the online version at https://doi.org/10.1016/bs.aivir.2023.06.002). Bar 20 μm.

While usefulness of RI sections in providing the cellular context for VF fluorescence is clear from Fig. 2, we were hoping to detect VFs in 3D RI map without the need for fluorescence. Fig. 4B shows 2D overlay of the central fluorescence section and the corresponding RI rendering in which four well defined round VF objects are identified. There is no apparent coincidence of the fluorescence with areas of higher RI which would be expected for places with concentrated viral components and RNA. The same conclusion is reached when the full 3D volume is rendered as RI density (Fig. 4C). This may be due to the relatively small size of these VFs (~1 μm or less) and perhaps lack of clear, sharp boundary between the VF interior and the cytoplasm.

In Figure 4DE we illustrate the key advantage of RI imaging over fluorescence when visualizing progress of infection over longer period, i.e., hours to days. In this experiment we monitored the cell culture continuously after infection and scanned the field of view for the first appearance of multinucleated syncytia. After 21 h.p.i. we zoomed onto one such area with a small cluster of multinucleated cells (Fig. 4D, boxed) and observed the spread of infection by cell fusion for the next 7 h. At the end of this period (i.e., 28 h.p.i.) most of the field of view is engulfed by a single or a few syncytia (Fig. 4E) with densely packed nuclei. The accompanying video (Supplementary Video 2 in the online version at https://doi.org/10.1016/bs.aivir.2023.06.002) shows that cell fusion events are abrupt, accompanied by rapid nuclear movement, and result in cytoplasmic volume reduction.

In summary, RI imaging provides three-dimensional cellular context to concurrent fluorescent imaging of viral replication. In addition, time-lapse RI series are suitable for observation of infection progress and spread within tissue with exquisite time (2 s) and spatial resolution (better than 400 nm) over hours to days without discernible phototoxicity. However, RI maps alone do not seem sufficient for label-free identification and localization of viral factories. Thus, refractive index alone is not sufficient to robustly discern this type of neoorganelles from the surrounding cytoplasm and label-free localization will need a multiparameter, information rich imaging technique. One such technique is spectral imaging, a variant of which, namely Raman microscopy, is discussed in the next section.

5. Confocal Raman microscopy

Most optical techniques rely on either generic contrast such as subtle changes in refractive index (phase contrast) or specific labelling with dye or fluorophore. The former delineates object boundaries rather

non-specifically while the latter indicates the presence of a specific component or tag, such as labeled protein or lipids which needs to be introduced to the sample. In addition, due to the broad nature of emission bands fluorescence imaging is generally limited to only a few concurrent spectral channels. Confocal Raman microscopy (CRM), on the other hand, relies on vibrational spectra of biomolecules with much sharper spectral features and thus provides richer information about the local chemical composition without the need for labelling. Raman spectroscopy and microscopy became a popular technique in life sciences because it requires little or no sample preparation and is compatible with water as a solvent. Raman spectroscopy and CRM has been widely used in biochemical, biophysical, biomedical research (Kann et al., 2015; Tuma, 2005) as well as for quality control of biopharmaceuticals (Buckley and Ryder, 2017).

CRM is a contactless, non-invasive, and often non-destructive imaging method that combines molecular specificity of Raman spectroscopy with a spatial resolution of confocal optical microscopy (Dieing et al., 2011). Raman spectroscopy is based on an inelastic scattering of photons on molecular vibrations, the so-called Raman scattering (Shipp et al., 2017). The frequencies (reported as wavenumbers using cm^{-1} units) of inelastically scattered photons provide information about the collective vibrational motions of atoms in molecules. Since the vibrational frequencies depend on the masses of the atoms within the molecule, the molecular structure and the strength of the chemical bonds, the Raman spectrum is a characteristic feature of the molecule in question, a kind of spectroscopic fingerprint or a barcode. This property, which is inherent to all methods of vibrational spectroscopy, i.e., Raman spectroscopy as well as infrared absorption, is referred to as molecular specificity. Change in the covalent structure of the molecule as well as formation of hydrogen bonds, isotopic exchange (e.g., deuteration) and conformational changes (e.g., formation of α-helices, DNA melting) are reflected in the positions and/or intensities of the Raman bands (Tuma et al., 1998). In general, chemically and structurally different types of molecules (e.g., phospholipids, proteins, polysaccharides or nucleic acids) provide different Raman fingerprints (Fig. 5, Table 2) by which they can be identified.

Biological macromolecules that possess the same repeating unit in their polymer backbones (e.g., peptide bond in proteins) or are made of similar building blocks (e.g., nucleotides in nucleic acids) often exhibit similar spectral features, so called marker bands or characteristic vibrations. The backbone specific markers, such as Amide *I* and Amide III in protein spectra

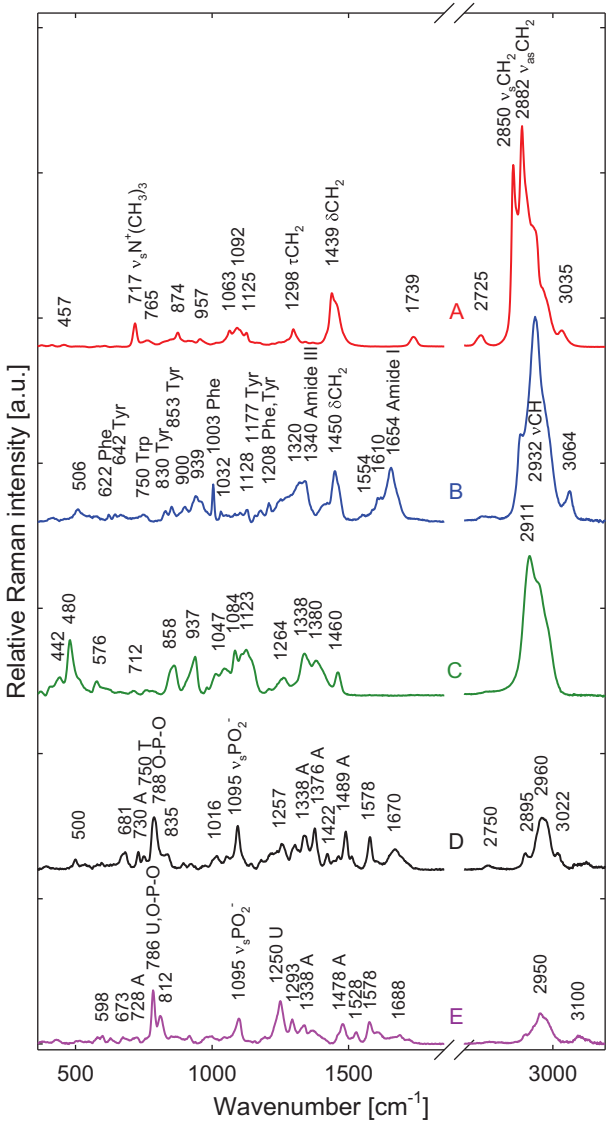

Fig. 5 Reference Raman spectra of selected biomolecules present in cells: partly unsaturated phospholipid (A), protein (B), glycogen (D), DNA (D) and RNA (E). The spectra are corrected for the water contribution to better display the details of the C–H and C–O stretching vibrations (2700–3150 cm^{-1}) that overlap with the water signal in the cells. For clarity, the spectra are normalized to have comparable maxima in the region of characteristic vibrations. ν – stretching mode; δ – deformation mode; τ – twisting mode; Tyr – tyrosine, Trp – tryptophan; Phe – phenylalanine; A – adenine; G – guanine; C – cytosine; T – thymine; U – uracil.

Table 2 Wavenumbers of the major bands identified in the Raman spectra of viral factories and their assignment to the basic biomolecules.

Wavenumber [cm^{-1}]	Biomolecule	Assignment [a]	References
478–480	Polysaccharides	Glycogen	Wiercigroch et al. (2017)
620–622	Proteins	Phe	Hernández et al. (2013), Tuma (2005)
642	Proteins	Tyr	Hernandez et al. (2016), Tuma (2005)
715–717	Phospholipids	$\nu_s(N^+–(CH_3)_3)$	Czamara et al. (2015), Kruglik et al. (2019)
721–730	Nucleic acids	Ring breathing of A	Kruglik et al. (2019)
750–758	Nucleic acids; Proteins	Ring breathing of T; Ring breathing of Trp	Benevides et al. (2002), Tuma (2005)
782–786	Nucleic acids	Phosphodiester O–P–O	Kruglik et al. (2019)
830	Proteins	Tyr Fermi doublet	Hernandez et al. (2016), Tuma (2005)
850–853	Proteins; Polysaccharides	Tyr; Glycogen	Tuma (2005), Wiercigroch et al. (2017)
936–939	Proteins; Polysaccharides	Glycogen	Wiercigroch et al. (2017)
1002–1005	Proteins	Phe	Hernández et al. (2013), Tuma (2005)
1034	Proteins	Phe; metal complexes of pyrophosphates	Hernández et al. (2013), Tuma (2005)
1084–1086	Polysaccharides	Glycogen	Wiercigroch et al. (2017)
1095–1100	Nucleic acids	Phosphodioxy $\nu_s(PO_2^-)$	Kruglik et al. (2019)
1127–1130	Lipids; Polysaccharides	ν(C–C); Glycogen	Czamara et al. (2015), Wiercigroch et al. (2017)
1156	Proteins	ν(C–C); ν(C–N); $\delta(CH_3)$	Tuma et al. (1996)

1175–1177	Proteins	Tyr	Hernandez et al. (2016), Tuma (2005)
1208	Proteins	Phe; Tyr	Hernandez et al. (2016), Hernández et al. (2013), Tuma (2005)
1254–1260	Proteins; Lipids	Amide III	Maiti et al. (2004)
1300–1302	Lipids	$\tau(CH_2)$	Czamara et al. (2015)
1330–1340	Nucleic acids; Polysaccharides; Proteins	Trp; A	Kruglik et al. (2019), Tuma (2005)
1442–1448	Lipids; Proteins	$\delta(CH_2)$	Tuma (2005), Wu et al. (2011)
1580–1585	Lipids; Proteins	Phe; Trp	Hernández et al. (2013), Tuma (2005)
1623	Proteins	Trp	Kruglik et al. (2019)
1653–1656	Lipids; Proteins	ν(C=C); Amide I	Czamara et al. (2015), Tuma (2005)
1739–1742	Lipids	ν(C=O) in triacylglycerols	Czamara et al. (2015)
2558	Proteins	ν(S–H)	Deniz et al. (2022), Tuma (2005)
2725	Lipids		Czamara et al. (2015)
2850	Lipids	$\nu_s(CH_2)$ in triacylglycerols	Czamara et al. (2015)
2880–2885	Lipids	$\nu_{as}(CH_2)$ in triacylglycerols	Czamara et al. (2015)
2930–2936	Lipids	$\nu_s(CH_3)$ in triacylglycerols and membrane lipids	Czamara et al. (2015)
3060–3065	Lipids	ν(C=CH)	Czamara et al. (2015)

[a] ν – stretching mode; δ – deformation mode; τ – twisting mode; Tyr – tyrosine, Trp – tryptophan; Phe – phenylalanine; A – adenine; G – guanine; C – cytosine; T – thymine; U – uracil.

(Fig. 5), result from coupled and delocalized vibrations of the polymer backbone (Table 2). The position of backbone marker bands is often sensitive to backbone conformation (Nemecek et al., 2013), allowing to discern proteins with different folds. On the other hand, intensities of repeating side chain marker bands (e.g., amino acids, nucleotides) reflect the composition. Of these, Raman contribution from aromatic side chains and nucleic acid bases is particularly strong due to their high polarizability of delocalized π-electrons. These simple principles and a wealth of accumulated spectra and assignments (Table 2) can be used to interpret Raman signatures of relatively complex viruses containing phospholipid membranes and multiple protein shells (Li et al., 1993; Tuma et al., 1996). However, such process is limited to in vitro conditions and requires demanding preparation of subviral particles (Bamford et al., 1993; Walin et al., 1994). Thus, a different approach is needed for analysis of complex mixtures such as that of cytoplasm and other cellular compartments.

To reliably discern different molecular species in complex mixtures, a wider range of Raman bands is to be considered and compared quantitatively using chemometric multivariate methods. This is usually done through singular value decomposition or a non-negative matrix factorization (Shipp et al., 2017) and these methods exploit spectral variations across the entire imaged volume or plane. They rank the spectral components by their contribution to image variation and yield their spatial distributions (relative intensities) across the image. Factorization can further be constrained to minimize spatial overlap of spectral components. When this is achieved the spatial distributions of the most significant components can be used for image map segmentation according to their prevailing Raman spectra which in turn reflect their chemical composition. As a result, one obtains an image map segmented according to "chemical" contrast.

To obtain the input spatially resolved Raman spectra, confocal microscope equipped with a high numeric aperture objective is used and the effective sampling volume is reduced to femtoliters (Dieing et al., 2011). By scanning the confocal volume and acquiring a full Raman spectrum at each point the chemical composition of the microscopic content and its spatial variability can be studied with sub-micron resolution. However, given the low intrinsic intensity of Raman signal, full spectral scanning is slower compared with that of typical confocal fluorescence microscope. Thus, cells are usually fixed prior to CRM to avoid cell movement during scanning and allow for longer accumulation time of spectra.

Despite its lower sensitivity CRM is suited for cell imaging because of the high intrinsic concentration of biomolecules within the cytoplasm and organelles. By the same argument CRM shall be applicable to spectral imaging and monitoring the processes of liquid-liquid phase separation and VF and virus formation inside virus infected cells (Yakubovskaya et al., 2021). However, there are two principal obstacles which make label-free Raman detection of VFs difficult. First, the Raman fingerprint of VFs is not known and might also depend on the stage of infection (e.g., early versus late stages). Second, human or mammalian cells are too large (tens of microns) compared to the average size of VF (~1 μm) for being scanned in their entirety with high enough resolution in a reasonable experimental time. Both problems can be solved by using *apriori* information on the location of VFs within the cell to identify the region of interest. As demonstrated above such information can be obtained by wide field fluorescence with the help of appropriate cell lines (or recombinant viruses) expressing fluorescently tagged marker protein (in our case ARV σNS-C-mCherry or RV NSP5-eGFP).

Raman mapping was done using an upright confocal Raman microscope WITec alpha300 RSA (WITec, Germany) equipped with the 60× water-immersion objective UPlanSApo, NA 1.2 (Olympus, Japan) and optical-fiber-connected spectrographs UHTS300 and UHTS400 (WITec, Germany) with CCD cameras (Andor, Ireland) optimized for detection in the visible and near-infrared region, respectively. The 532 or 647 nm lasers with the excitation power of approximately 20 mW at the focal plane were used. The cells were cultivated in round 35/10 mm cell culture dishes with glass bottom (μ-dish by Ibidi) as described above in Section 3.2. The cells were fixed with 2% glutaraldehyde, twice washed with PBS buffer (in order to eliminate any contributions to spectra), and overlaid by 1–2 mm thick layer of the 1% low-temperature-melting agarose dissolved in PBS. Finally, a 20 mm glass coverslip was placed at the top surface of the agarose and sealed with a CoverGrip sealant (Biotium, USA). After such mechanical stabilization, the culture dish could be turned upside down and measured with the upright microscope (Fig. 6) without the risk of the detachment of the cells from the glass window and dehydration. This also provided biological containment for the potentially infectious material.

As wide field fluorescence provides only localization in the specimen (x-y) plane the location of VFs along the axial z-direction remains uncertain, especially for small objects with dimensions close to the diffraction limit.

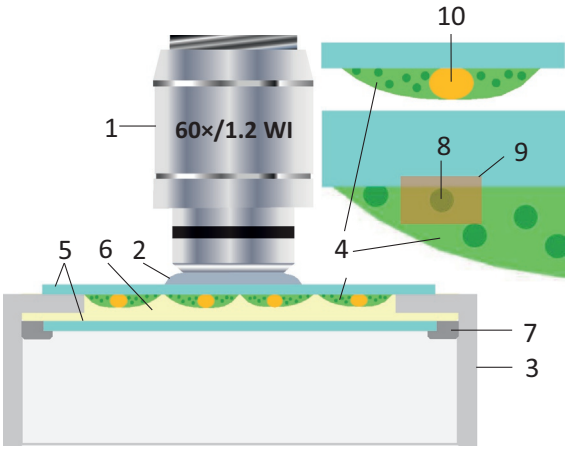

Fig. 6 Schematic of the vertical scanning of infected cells cultivated in cell culture dishes. Immersion objective (1), immersion liquid – water (2), cell culture dish (3), cells (4), coverslips (5), a layer of low-melting agarose (6), sealant (7), fluorescently labeled VFs (8), x-z plane used for initial spectral scan (9), cell nucleus (10).

Thus, it is more practical to perform initial Raman spectral scan of such objects in 2D axial x-z plane instead of x-y (Fig. 6). MA104 cells expressing RV protein NSP5 tagged with eGFP and infected with bovine rotavirus in (Fig. 7), we first used GFP fluorescence to laterally localize VFs (panel A). Raman mapping was then performed preferentially in the x-z plane (Fig. 7A) with a scanning step of 200 nm in both directions and a voxel size of 1 μm^3, using an integration time of 0.07 s per voxel. A typical area of 16 m × 8 m (z-direction) was measured. Data were analyzed using WITec Project Six Plus ver.6.0.6 software (WITec, Germany) by implementing the following steps: cosmic ray removal, cropping of the spectral edges affected by detector margins, background subtraction (approximated by a third order polynomial), and spectral unmixing with the True Component Analysis (TCA) tool (WITec, Germany). Three significant, spatially separated components (Fig. 7B–D left) with different spectra (Fig. 7B–D right) were identified and used to segment the image (Fig. 7E). The assignments of VF segment (red) were done through coincidence with fluorescence, while the lipid component (yellow) was discerned based on the characteristic Raman fingerprint (e.g., strong bands at 1085, 1300 cm^{-1} from phospholipids, Table 2). The rest of the map (green) was assigned to cytoplasm owing to its high protein content (Amide I and III bands, Table 2).

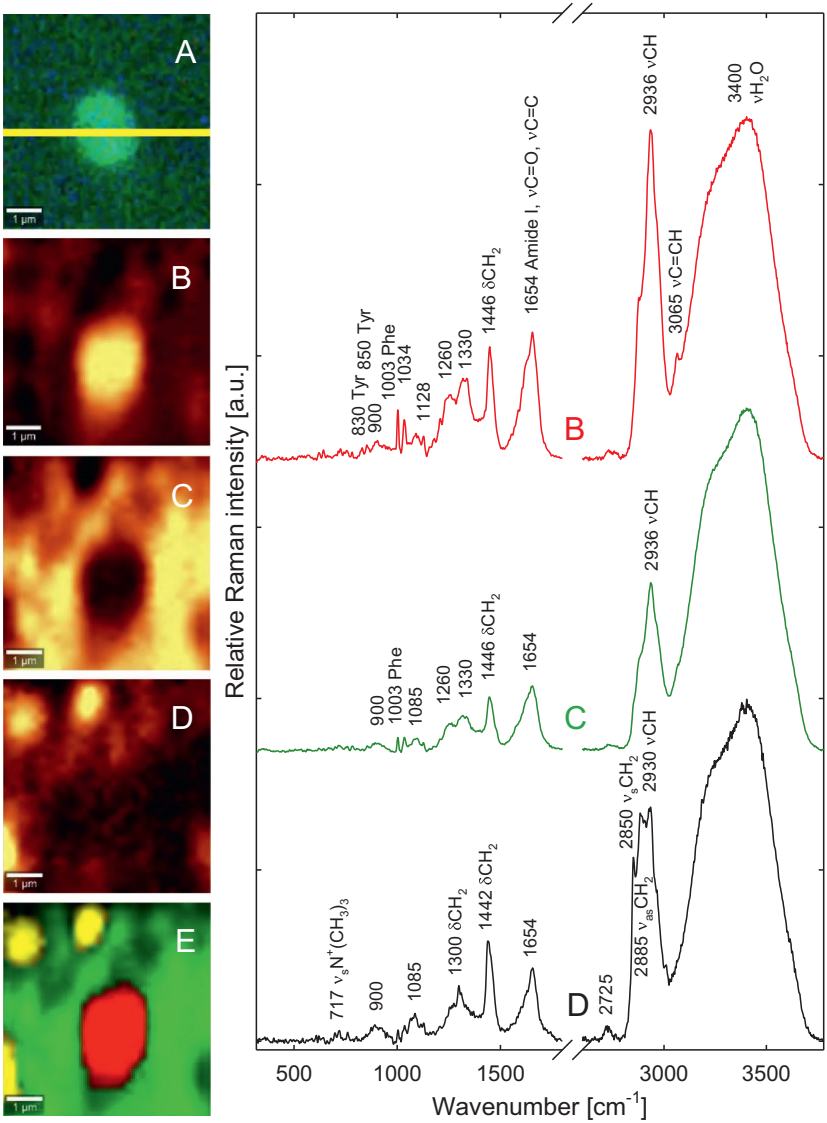

Fig. 7 Rotavirus viral factories (8 h.p.i), incorporating NSP5-eGFP that is stably expressed in MA104 cells, were located by wide-field fluorescence microscopy in fixed cells (A). The horizontal yellow line indicates the lateral Raman scanning span along x axis. Left panels (B–D) represent the spatial distributions of the three most significant spectral components obtained by TCA (relative intensity scale dark to bright). (E) After segmentation pixels belonging to the individual segmented domain were delineated using spatial loading threshold and colored. Raman spectra from all pixels belonging to each domain were integrated and normalized with respect to the broad intense water band between 3000 and 3750 cm^{-1} (right panel B–D).

A hallmark of neoorganelles that are formed by LLPS is the increased concentration of selected components in their interior. Raman spectra offer a quantitative way to compare relative concentration of different molecular components within the segmented regions. Due to high molar content of water the integrated spectra exhibit contribution from water: a broad intense band between 3000 and 3750 cm^{-1} is assigned to OH stretching vibration a weaker broad feature centered at 1640 cm^{-1}) The former, which has little overlap with spectral contributions from biomolecules, can be used to normalize the spectra. Spectra of biomolecules exhibit a strong feature between 2800 and 3000 cm^{-1} that is assigned to C–H stretching vibrations and thus its intensity is proportional to the amount of organic matter in the sample. Hence, the intensity of this feature in the normalized spectra reflects the relative concentration of biomolecules within the segmented region. As shown in Fig. 7 right, the VF body is very dense, having a concentration of biomolecules at least twice that of the cytoplasm (right panel B versus C). However, the spectra (B and C) are rather similar, being dominated by protein markers, and this suggests protein-rich composition of both compartments. On the other hand, lipid particles (D) are clearly different. Although VFs contain RNAs, we could not detect the contribution from nucleic acids. Hence the molar fraction of RNA in RV viral factories may be relatively small. This result is consistent with the rotavirus VF formation being initially protein driven and independent of the RNA, which gradually accumulate in viroplasms over the course of infection (Geiger et al., 2021).

Although we initially located a region of interest by VF fluorescence, it is clear that the Raman spectra of viroplasms differ substantially from both the cytoplasm (mainly due to higher protein density), as well as from lipid-containing vesicles/droplets (due to their distinct characteristic spectrum) making it feasible to be detected by label-free CRM imaging. To explore the robustness of the TCA methodology, we selected a wider area encompassing part of a nucleus, and we performed an x-y scan at a fixed depth below the cover slip (Fig. 8). In this case, TCA identified five components, including that of VFs. Note that due to the wider scan area and the presence of multiple components, there is a significant "bleed through" between the pseudo-spectral channels that are defined by the true component. However, cell structures (e.g., the nucleus, panel C, the nuclear envelope and a part of the ER, E) and VF (panel D) are clearly discernible within the label-free images.

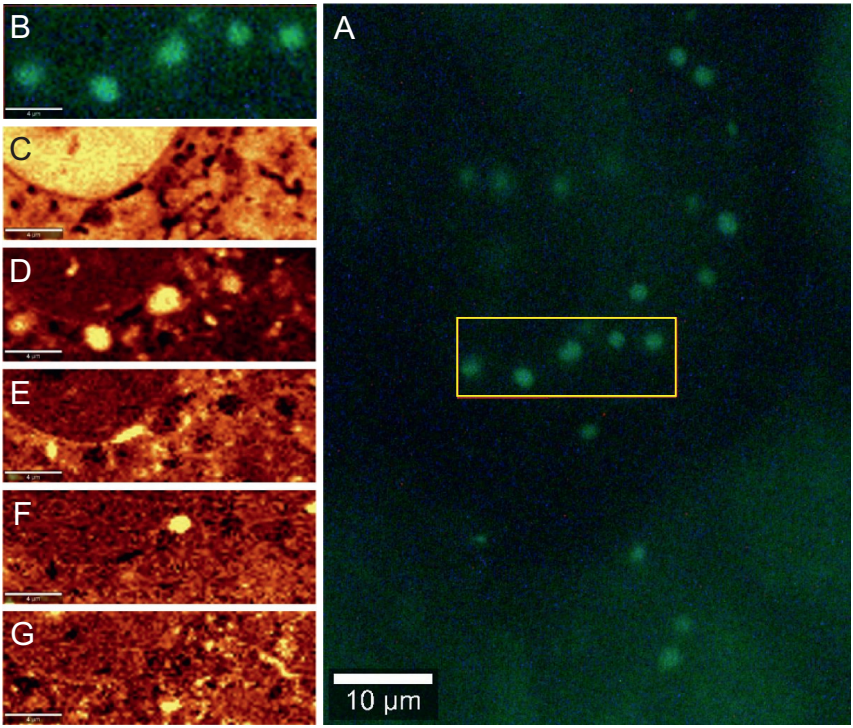

Fig. 8 The VFs localized in MA104 cells by GFP fluorescence (A). The yellow rectangle shows the laterally (x-y) scanned area (B). The decomposition of Raman spectra acquired from the scanned area disclosed five spectrally distinct structures: nucleus (C), VFs (D), lipid-rich particles (E), glycogen granules (F), and protein rich cytoplasmic regions (G) differing in their Raman spectra from the rest. The respective Raman spectra are depicted in Fig. 9 under the same labeling as the corresponding Raman chemical maps.

Unlike fluorescence staining and tagging, which provide highly specific contrast, it is the cognate Raman spectra and the spatial cellular context which both need to be considered to sort out the identity of the segmented regions (Fig. 9). For example, the highest spatial density in panel C maps onto an area which looks like the nucleus while the cognate spectrum contains contribution from nucleic acids. However, due to spectral and compositional similarities, cytoplasm also exhibits significant densities assigned primarily to the nucleus. Hence, as is common for any density map interpretation, the segmentation boundaries depend on the selected threshold. Perinuclear, lipid containing densities (panel E) can be assigned to the nuclear envelope and ER due to their specific Raman signature

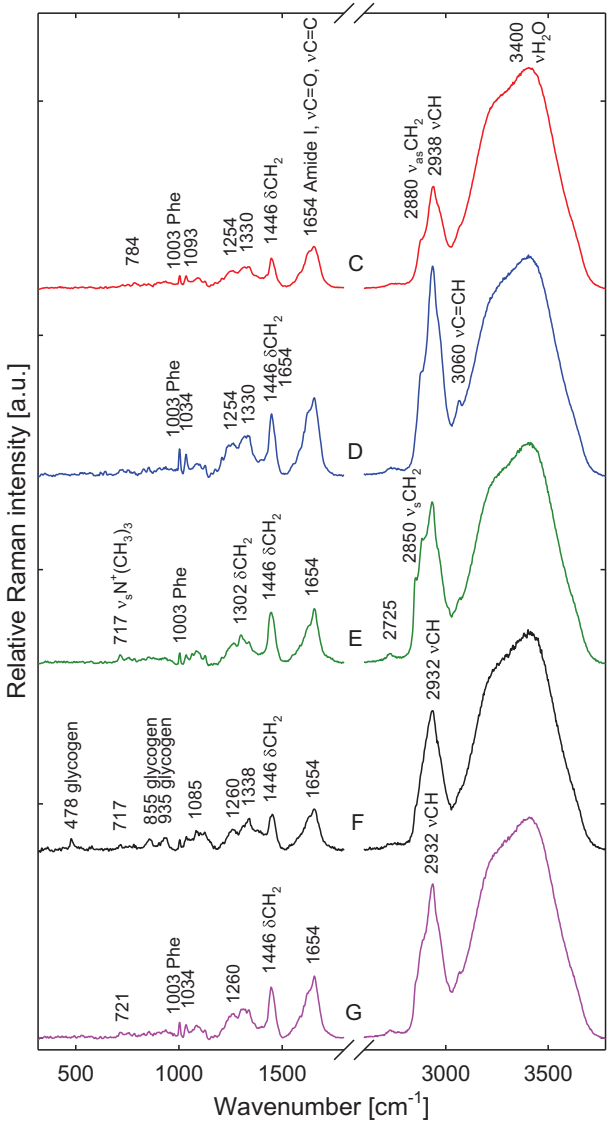

Fig. 9 Raman spectra corresponding to the five distinct intracellular regions visualized in segmented Raman maps (Fig. 8). Spectra are normalized with respect to the Raman band of water (ca 3400 cm-1). Based on Raman markers of various biomolecules (Table 2) and spatial information from Raman maps, spectra can be assigned to the nucleus (C), VFs (D), lipid-rich particles (E), glycogen granules (F), and protein-rich cytoplasmic regions (G).

and cellular location. VFs are, as seen above, mostly distinguished by their high protein content in comparison to other cellular features (Fig. 9D). The spectrum in Fig. 9F illustrates the power of label-free chemical mapping by detecting a glycogen granule. Such granules are often overlooked in virological studies, yet their imaging may provide the important local cellular context for VF formation and virion assembly. In addition, protein-rich regions were localized in cytoplasm (Figs. 8 and 9, panel G) but their identities cannot be discerned from Raman spectra and from their spatial distribution.

Label-free detection successfully mapped four out of five fluorescent VF regions (Figure 8BD). The remaining is still somewhat discernible within the Raman TCA map with low intensity, most likely being located just outside the selected z-plane. Nevertheless, this still allowed us to compare variations in the average spectra obtained for each of these regions (Fig. 10, red spectra) and compare those with variations among spectra from similarly

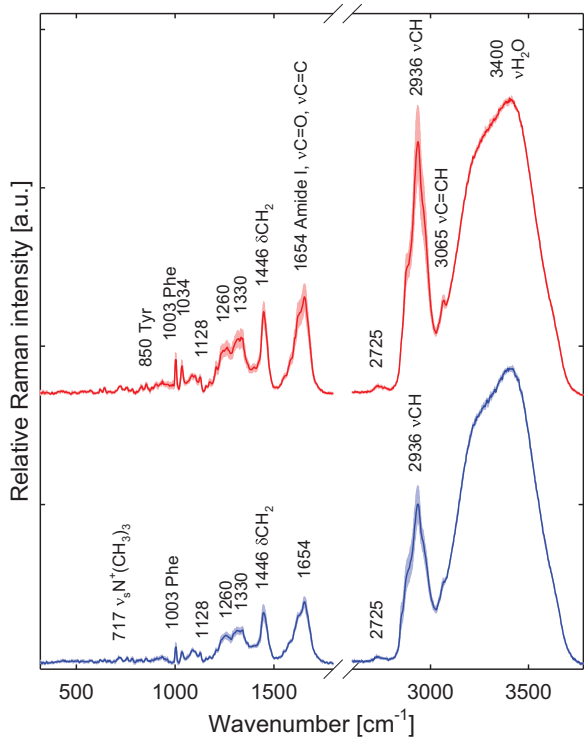

Fig. 10 Raman spectra illustrating spectral variability of five VFs (red line) and their cytoplasmic surroundings (blue line). Spectra are normalized with respect to the intensity of the O–H stretching band of water.

sized cytoplasmic regions (Fig. 10, blue spectra). The latter exhibit much less variation both in composition as well as biomolecular concentration (vis-a-vis Raman band of water, see above). The spectral variation among VFs is larger than in the surrounding cytoplasm but in all the sampled regions exhibited concentrations significantly above that of the cytoplasm. In the light of the substantial spectral variation among VFs any correlations between, e.g., the progress of infection or VF morphology and the Raman signature would require rigorous statistical analysis which goes beyond difference spectroscopy, a commonly used tool for detecting and interpreting spectral changes in purified samples (Benevides et al., 2002).

The above discourse suggested that, at least for rotavirus, VFs can be detected by label-free Raman confocal imaging which in turn relies on their high protein density. Having developed BHK-21 cell line stably expressing σNS-C-mCherry VF marker for following ARV infection (see Section 3 above) we were able to localize VFs in a late (21 h.p.i.) multinucleated syncytium (Fig. 11A) and perform CRM volume (x-y-z) scan in the area delineated in Fig. 11B (x-y projection).

The spectra were collected and processed as described above for RV and resulting spectral volume was decomposed into three significant spatio-spectral components (Fig. 12). The volume encompassed VFs (spectrum A and red density in Fig. 12) with high protein concentration with respect to that of surrounding perinuclear and nuclear region

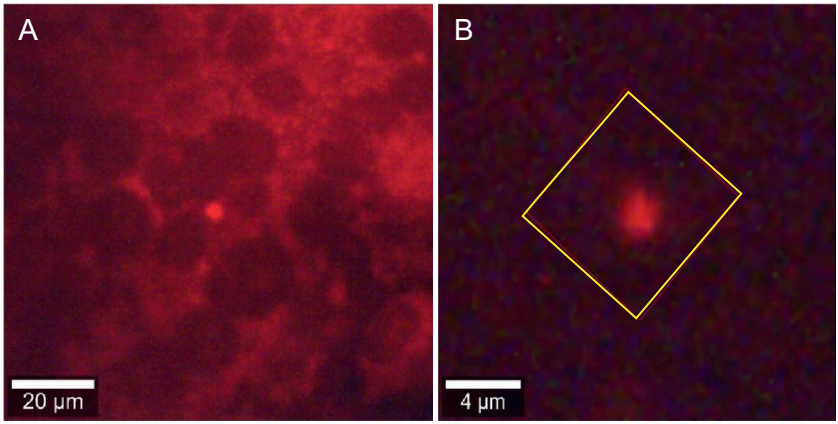

Fig. 11 The ARV viral factories (24 h.p.i.) labeled with σNS-C-mCherry and visualized by wide-field fluorescence microscopy (A, B). The yellow rectangle in panel B indicates the position where the z-stack of 16 x-y Raman images was obtained. The vertical step was 500 nm.

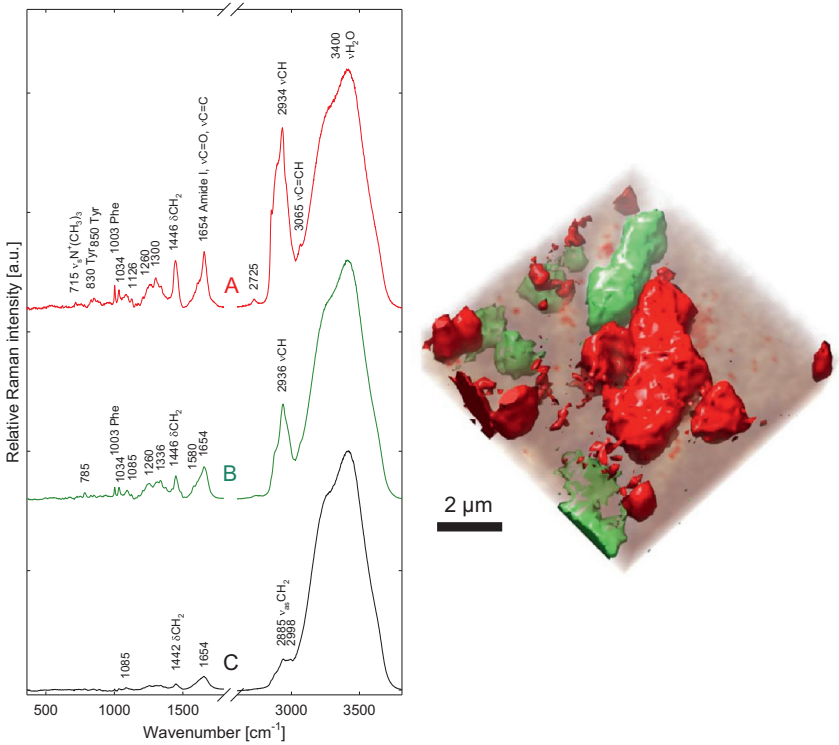

Fig. 12 (Left) Raman spectra of three components revealed by a joint spectral decomposition of 16 Raman maps obtained from z-stacking. The 3D spectra are normalized with respect to the intensity of the O–H stretching band of water. The red spectrum (A) corresponds to VF, the green one (B) to nuclei limiting the area with VF, and the black (C) is largely due to medium with low-melting agarose covering the layer of the cells. (Right) Three-dimensional map of the scanned volume colored by density of spectral components; VFs – red, perinuclear cytoplasm and nuclear regions – green, cytoplasm and mounting agarose – translucent. 3D rendering done with UCSF Chimera https://www.rbvi.ucsf.edu/chimera (Goddard et al., 2018).

(component B, green). In addition, the scan contained contributions from the cell periphery and beyond, including that of the PBS buffer and the mounting agarose (component C, translucent in 3D map). In addition to the few smaller, roughly spherical VFs, a large VF with asymmetric appearance was found. This morphology is clearly different from the spherical VFs observed for RV and could be due to the late stage of infection. While this assertion will need further substantiation it illustrates the power of CRM being able to provide information on morphology in three-dimensional context of the cell.

In summary, Raman microscopy can identify VFs in infected cells without the need for label, chiefly due to their high protein concentration. This seems to be the case for both RV and ARV, suggesting the method be applicable to other members of the *Reoviridae* family. Three-dimensional scans also provide information about VF morphology which may significantly deviate from the spherical during late stages of infection. In addition, CRM provides structural context in 3D according to chemical contrast which is more discerning than refractive index and this feature is particularly useful for detecting VF-proximal membranes that are thought to play important role in the morphogenesis of many viruses.

6. Electron microscopy

EM has been an essential tool of virology for many decades, recently being augmented by advances in direct electron detectors and cryogenic imaging. Both transmission (TEM) and scanning (SEM) methods can provide structural information about the course of infection that is complementary and superior in resolution to the above discussed optical methods. Standard TEM can visualize virions and sub-viral particles in stained thin sections of infected cells and can provide ultrastructural context of readily recognizable cellular structures and organelles (e.g., microtubules, mitochondria, endoplasmic reticulum and lipid vesicles). These methods are now extended to volume imaging, e.g., by serial sectioning, electron tomography (ET) and focused ion beam scanning EM. Here, we illustrate the complementarity of TEM imaging and serial section tomography to the optical methods discussed above. We limit our discourse to samples prepared by standard chemical fixation and heavy metal staining. More advanced correlative techniques and advanced EM sample preparation methods were recently used to visualize key steps of MRV infection and egress (de Castro et al., 2021; Sachse et al., 2019).

6.1 Stained ultrathin sections reveal viral factories and virion arrays

For EM, infected cell cultures were imaged by HTM (RI only to avoid fluorescence associated phototoxic effects) and samples were fixed at different times post infection by a mixture of aldehydes (2% formaldehyde, 2.5% glutaraldehyde in buffer). After 24 h in the fixing solution, the sample was put into several consecutive staining solutions (2% aq. OsO_4, 2.5% aq. potassium ferricyanide, 1% aq. thiocarbohydrazide, 2% aq. OsO_4, 1% aq. uranyl

acetate) with washing between the staining steps. The glass bottom of the dish was subsequently cut out and transferred into a whole glass petri dish prior to drying with ethanol and acetone. The dehydrated samples were infiltrated with Epon resin in acetone (1:2–1:1–2:1 and 100% Epon) and clean Epon resin blocks were placed directly onto the sample and left to polymerize at 60 °C for 48 h. After the polymerization, the glass was removed from the sample by heat shock cycles (liquid nitrogen and hot water) and the sample-containing surface was trimmed into a pyramid by a razor blade and sectioned on a diamond knife into 70–80 nm ultrathin sections. The sections were stained with 10% uranyl acetate (in ethanol) and 1% lead citrate (in water) and carbon coated before visualization in a 120 kV transmission electron microscope (Jeol 1400Flash).

Fig. 13A shows an ultrathin section of ARV infected BHK-21 cells late in infection (24 h.p.i.) in which three nuclei are clearly visible in what must be a part of larger multinucleated syncytium. A closer look at the cytoplasmic area between nuclei (Fig. 13B) reveals fragmented arrays of tightly packed virions that can be identified from their size (85 nm) and regular shape. Among those arrays are densely stained regions which are tentatively assigned to viral factories since they resemble the irregular shapes and size of VFs seen in similar internuclear locations by CRM in fixed cells (Fig. 12) and by HTM in live cells (21 h.p.i., Fig. 2B).

This demonstrates the utility of performing simple thin section TEM in parallel with other techniques and opens up avenues to answer questions about how virions egress from VFs and whether and how VFs are being remodeled from the initial spherical and fluid shape to the asymmetric, larger bodies seen late in infection at multiple length scales. As demonstrated by CRM answering these questions may be facilitated by 3D imaging, i.e., going from a single thin section TEM to serial section electron tomography, as described in the next section.

6.2 Serial section electron tomography

BHK-21 cells were fixed late in infection (24 h.p.i.), embedded in resin as described above and cut into 70 nm thick sections that were placed on a mesh grid and carbon coated. Transmission electron microscope Jeol 2100 F equipped with Gatan K2 direct electron detector was used to search for viral inclusions and subsequent tomographic data acquisition. The data for the serial electron tomogram were collected automatically using SerialEM (Mastronarde, 2005) from two consecutive sections, each as a

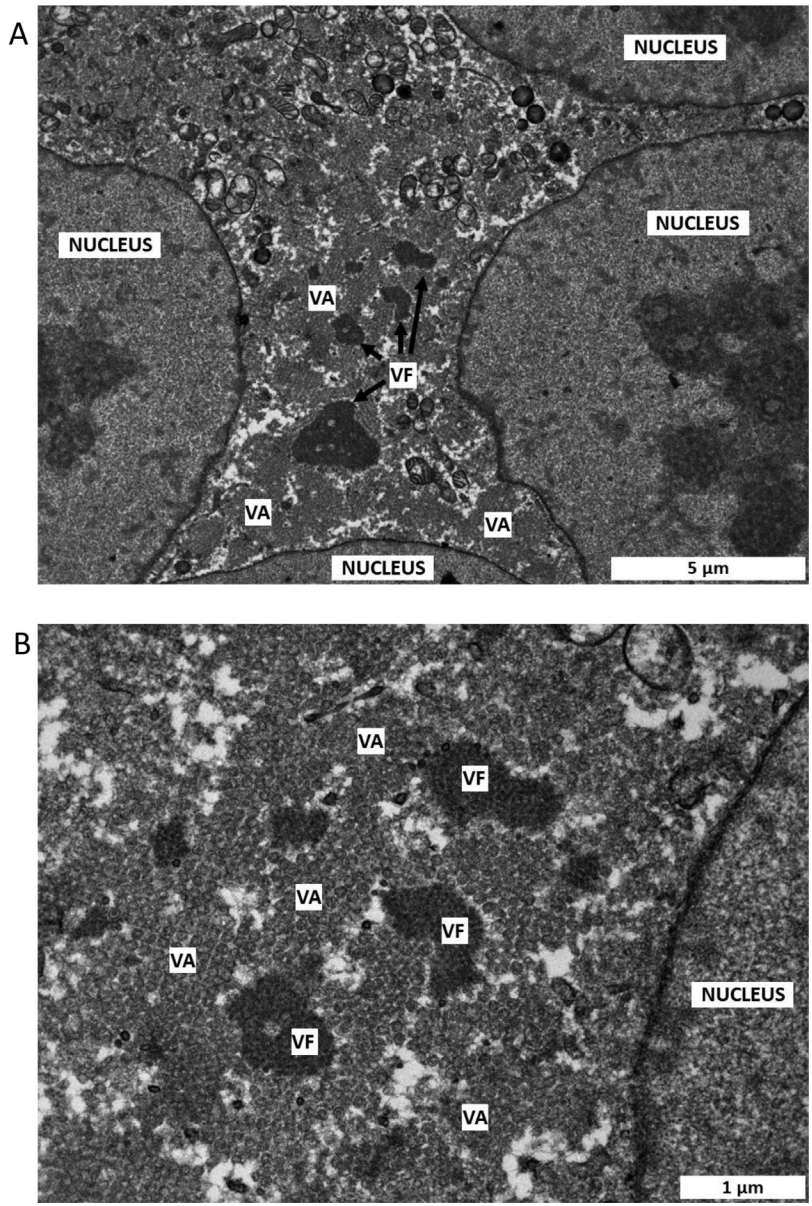

Fig. 13 (A) TEM image of ARV (S1133 strain) infected BHK-21 multinucleated syncytium fixed 24 h.p.i. and sectioned (80 nm thickness), contrasted with uranyl acetate and lead citrate and imaged by transmission electron microscopy (120 kV, Jeol 1400Flash). (B) A detailed view of the cytoplasmic area between nuclei in panel A. VA - viral array, VF – viral factory, scale bars 5 μm (A) and 1 μm (B).

single-axis tilt series in the range ±70 with step 1 (141 images in total). Etomo software package was used for the tomogram reconstructions, stitching, and anisotropic diffusion filtering (Mastronarde and Held, 2017).

Fig. 14A shows a section from a tomogram containing arrays of multi shelled virions. Two consecutive sections through the selected area of

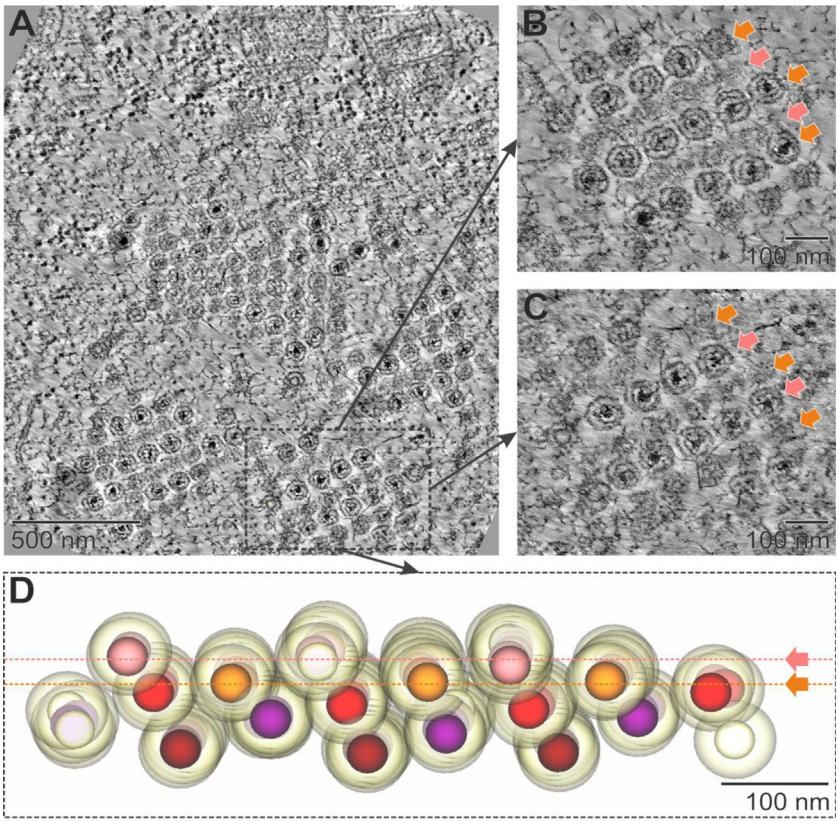

Fig. 14 BHK-21 cells infected with ARV strain S1133 24 h.p.i. (A) A central section from two stitched serial tomograms representing a ~115 nm thick reconstructed volume with an isotropic pixel/voxel size of 0.67 nm. The dashed rectangle depicts area of interest for enlarged slices in panels B and C. (B and C) Two tomography slices with a position difference of 23.45 nm along z-axis. The orange and mauve arrows point to virions located in neighboring planes as viewed from the top of the tomogram. (D) A side view of 3D lattice packing model created from the total volume from area defined by the dashed rectangle in panel A. Virions belonging to different planes are colored mauve, orange, red, purple and brown, respectively. Virions which appear to be void of RNA are white irrespective of the layer they belong to. See the accompanying video (Supplementary Video 3 in the online version at https://doi.org/10.1016/bs.aivir.2023.06.002) for 3D details. Model and video creation were performed in the Imod software package (Mastronarde and Held, 2017).

tomogram (Fig. 14BC) reveals tight packing of virions in three-dimensional lattice. This is further substantiated by subsequent layers and interpreted in a lattice schematic (Fig. 14D) and accompanying video (Supplementary Video 3 in the online version at https://doi.org/10.1016/bs.aivir.2023.06.002). This shows that BHK-21 cells can produce the virus in quantities large enough to form 3D nanocrystals that fill the remaining cytoplasm between nuclei. However, this may be the result of compromised virus egress from these cells and infection of avian cell lines needs to be examined under similar condition. With the help of serial section ET we were able to detect what appears as empty virions within these nanocrystals but their fraction seemed rather small.

7. Concluding remarks

The past decade has seen the concept of liquid, membrane-less neoorganelles mature as they were shown to be involved in many cellular processes. Recently, LLPS was shown to be involved in the assembly of rotavirus and here we provide evidence that this may be the case also for avian reovirus. This suggests that the LLPS phenomena might be emerging as a common way to organize viral factories in cells and consequently, a new set of tools is needed to study the formation of these inclusions and virus assembly within. Multiscale, three-dimensional, and live cell imaging techniques are going to play a prominent role given the dynamic nature of VFs and liquid character of the interior.

Acknowledgments

This work was supported by European Regional Development Fund (grant no.: CZ.02.1.01/0.0/0.0/15_003/0000441) and Czech Science Foundation GACR 22-25396S. BC CAS core facility LEM is supported by MEYS CR LM2023050 Czech-BioImaging and OP VVV CZ.02.1.01/0.0/0.0/18_046/0016045. A.B. was supported by the Wellcome Trust [213437/Z/18/Z to A.B.]. Molecular graphics and analyses were performed with UCSF Chimera, developed by the Resource for Biocomputing, Visualization, and Informatics at the University of California, San Francisco, with support from NIH P41-GM103311.

References

Axelrod, D., Koppel, D.E., Schlessinger, J., Elson, E., Webb, W.W., 1976. Mobility measurement by analysis of fluorescence photobleaching recovery kinetics. Biophys. J. 16, 1055–1069.

Bamford, J.K., Bamford, D.H., Li, T., Thomas Jr., G.J., 1993. Structural studies of the enveloped dsRNA bacteriophage phi 6 of pseudomonas syringae by Raman spectroscopy. II. Nucleocapsid structure and thermostability of the virion, nucleocapsid and polymerase complex. J. Mol. Biol. 230, 473–482.

Benavente, J., Martinez-Costas, J., 2007. Avian reovirus: structure and biology. Virus Res. 123, 105–119.
Benevides, J.M., Juuti, J.T., Tuma, R., Bamford, D.H., Thomas, G.J., 2002. Characterization of subunit-specific interactions in a double-stranded RNA virus: Raman difference spectroscopy of the φ6 procapsid. Biochemistry 41, 11946–11953.
Bodelon, G., Labrada, L., Martinez-Costas, J., Benavente, J., 2002. Modification of late membrane permeability in avian reovirus-infected cells: viroporin activity of the S1-encoded nonstructural p10 protein. J. Biol. Chem. 277, 17789–17796.
Borodavka, A., Ault, J., Stockley, P.G., Tuma, R., 2015. Evidence that avian reovirus σNS is an RNA chaperone: implications for genome segment assortment. Nucleic Acids Res. 43, 7044–7057.
Borodavka, A., Desselberger, U., Patton, J.T., 2018. Genome packaging in multi-segmented dsRNA viruses: distinct mechanisms with similar outcomes. Curr. Opin. Virol. 33, 106–112.
Brandariz-Nunez, A., Menaya-Vargas, R., Benavente, J., Martinez-Costas, J., 2010a. Avian reovirus microNS protein forms homo-oligomeric inclusions in a microtubule-independent fashion, which involves specific regions of its C-terminal domain. J. Virol. 84, 4289–4301.
Brandariz-Nunez, A., Menaya-Vargas, R., Benavente, J., Martinez-Costas, J., 2010b. A versatile molecular tagging method for targeting proteins to avian reovirus muNS inclusions. Use in protein immobilization and purification. PLoS One 5, e13961.
Bravo, J.P.K., Bartnik, K., Venditti, L., Acker, J., Gail, E.H., Colyer, A., Davidovich, C., Lamb, D.C., Tuma, R., Calabrese, A.N., Borodavka, A., 2021. Structural basis of rotavirus RNA chaperone displacement and RNA annealing. Proc. Natl. Acad. Sci. U. S. A. 118, e2100198118.
Bravo, J.P.K., Borodavka, A., Barth, A., Calabrese, A.N., Mojzes, P., Cockburn, J.J.B., Lamb, D.C., Tuma, R., 2018. Stability of local secondary structure determines selectivity of viral RNA chaperones. Nucl. Acid Res. 46, 7924–7937.
Broering, T.J., Parker, J.S., Joyce, P.L., Kim, J., Nibert, M.L., 2002. Mammalian reovirus nonstructural protein microNS forms large inclusions and colocalizes with reovirus microtubule-associated protein micro2 in transfected cells. J. Virol. 76, 8285–8297.
Buckley, K., Ryder, A.G., 2017. Applications of Raman spectroscopy in biopharmaceutical manufacturing: a short review. Appl. Spectrosc. 71, 1085–1116.
Choi, W., Fang-Yen, C., Badizadegan, K., Oh, S., Lue, N., Dasari, R.R., Feld, M.S., 2007. Tomographic phase microscopy. Nat. Methods 4, 717–719.
Cotte, Y., Toy, F., Jourdain, P., Pavillon, N., Boss, D., Magistretti, P., Marquet, P., Depeursinge, C., 2013. Marker-free phase nanoscopy. Nat. Photon. 7, 113–117.
Czamara, K., Majzner, K., Pacia, M.Z., Kochan, K., Kaczor, A., Baranska, M., 2015. Raman spectroscopy of lipids: a review. J. Raman Spectrosc. 46, 4–20.
de Castro, I.F., Fernandez, J.J., Dermody, T.S., Risco, C., 2021. Electron tomography to study the three-dimensional structure of the Reovirus egress pathway in mammalian cells. Bio. Protoc. 11, e4080.
Deniz, E., Schmidt-Engler, J.M., Ulrich, K., Oberle, M., Wille, G., Bredenbeck, J., 2022. SH-it happens: S-H bonds as intrinsic 2D-IR labels in proteins. J. Chem. Phys. 157, 9.
Desmet, E.A., Anguish, L.J., Parker, J.S., 2014. Virus-mediated compartmentalization of the host translational machinery. MBio 5. e01463–14.
Dieing, T., Hollricher, O., Toporski, J., 2011. Confocal Raman Microscopy. Springer, Heidelberg.
Diestra, E., Fontana, J., Guichard, P., Marco, S., Risco, C., 2009. Visualization of proteins in intact cells with a clonable tag for electron microscopy. J. Struct. Biol. 165, 157–168.
Fernandez de Castro, I., Zamora, P.F., Ooms, L., Fernandez, J.J., Lai, C.M., Mainou, B.A., Dermody, T.S., Risco, C., 2014. Reovirus forms neo-organelles for progeny particle assembly within reorganized cell membranes. mBio, 5.

Geiger, F., Acker, J., Papa, G., Wang, X., Arter, W.E., Saar, K.L., Erkamp, N.A., Qi, R., Bravo, J.P., Strauss, S., Krainer, G., Burrone, O.R., Jungmann, R., Knowles, T.P., Engelke, H., Borodavka, A., 2021. Liquid-liquid phase separation underpins the formation of replication factories in rotaviruses. EMBO J. 40, e107711.

Goddard, T.D., Huang, C.C., Meng, E.C., Pettersen, E.F., Couch, G.S., Morris, J.H., Ferrin, T.E., 2018. UCSF ChimeraX: meeting modern challenges in visualization and analysis. Protein Sci. 27, 14–25.

Grande, A., Benavente, J., 2000. Optimal conditions for the growth, purification and storage of the avian reovirus S1133. J. Virol. Methods 85, 43–54.

Hernandez, B., Coic, Y.M., Pfluger, F., Kruglik, S.G., Ghomi, M., 2016. All characteristic Raman markers of tyrosine and tyrosinate originate from phenol ring fundamental vibrations. J. Raman Spectrosc. 47, 210–220.

Hernández, B., Pflüger, F., Kruglik, S.G., Ghomi, M., 2013. Characteristic Raman lines of phenylalanine analyzed by a multiconformational approach. J. Raman Spectrosc. 44, 827–833.

Hyman, A.A., Weber, C.A., Julicher, F., 2014. Liquid-liquid phase separation in biology. Annu. Rev. Cell Dev. Biol. 30, 39–58.

Kanai, Y., Kawagishi, T., Matsuura, Y., Kobayashi, T., 2019. In vivo live imaging of oncolytic mammalian Orthoreovirus expressing NanoLuc luciferase in tumor xenograft mice. J. Virol. 93, e00401–19.

Kann, B., Offerhaus, H.L., Windbergs, M., Otto, C., 2015. Raman microscopy for cellular investigations- -From single cell imaging to drug carrier uptake visualization. Adv. Drug Deliv. Rev. 89, 71–90.

Kaufer, S., Coffey, C.M., Parker, J.S., 2012. The cellular chaperone hsc70 is specifically recruited to reovirus viral factories independently of its chaperone function. J. Virol. 86, 1079–1089.

Kniert, J., Dos Santos, T., Eaton, H.E., Jung Cho, W., Plummer, G., Shmulevitz, M., 2022. Reovirus uses temporospatial compartmentalization to orchestrate core versus outercapsid assembly. PLoS Pathog. 18, e1010641.

Knipe, D.M., Howley, P.M., 2013. Fields Virology. Wolters Kluwer, Philadelphia.

Kopek, B.G., Perkins, G., Miller, D.J., Ellisman, M.H., Ahlquist, P., 2007. Three-dimensional analysis of a viral RNA replication complex reveals a virus-induced mini-organelle. PLoS Biol. 5, e220.

Kruglik, S.G., Royo, F., Guigner, J.M., Palomo, L., Seksek, O., Turpin, P.Y., Tatischeff, I., Falcon-Perez, J.M., 2019. Raman tweezers microspectroscopy of circa 100 nm extracellular vesicles. Nanoscale 11, 1661–1679.

Labadie, T., Sullivan, E., Roy, P., 2020. Multiple routes of bluetongue virus egress. Microorganisms 8, 965.

Lee, C.H., Raghunathan, K., Taylor, G.M., French, A.J., Tenorio, R., Fernandez de Castro, I., Risco, C., Parker, J.S.L., Dermody, T.S., 2021. Reovirus nonstructural protein sigmaNS recruits viral RNA to replication organelles. MBio 12, e0140821.

Li, T., Bamford, D.H., Bamford, J.K., Thomas Jr., G.J., 1993. Structural studies of the enveloped dsRNA bacteriophage phi 6 of pseudomonas syringae by Raman spectroscopy. I. The virion and its membrane envelope. J. Mol. Biol. 230, 461–472.

Liu, J., Yu, C., Gui, J.F., Pang, D.W., Zhang, Q.Y., 2018. Real-time dissecting the entry and intracellular dynamics of single Reovirus particle. Front. Microbiol. 9, 2797.

Maiti, N.C., Apetri, M.M., Zagorski, M.G., Carey, P.R., Anderson, V.E., 2004. Raman spectroscopic characterization of secondary structure in natively unfolded proteins: alpha-synuclein. J. Am. Chem. Soc. 126, 2399–2408.

Martinez-Costas, J., Grande, A., Varela, R., Garcia-Martinez, C., Benavente, J., 1997. Protein architecture of avian reovirus S1133 and identification of the cell attachment protein. J. Virol. 71, 59–64.

Mastronarde, D.N., 2005. Automated electron microscope tomography using robust prediction of specimen movements. J. Struct. Biol. 152, 36–51.
Mastronarde, D.N., Held, S.R., 2017. Automated tilt series alignment and tomographic reconstruction in IMOD. J. Struct. Biol. 197, 102–113.
Miller, C.L., Broering, T.J., Parker, J.S.L., Arnold, M.M., Nibert, M.L., 2003. Reovirus NS protein localizes to inclusions through an association requiring the NS amino terminus. J. Virol. 77, 4566–4576.
Mojzes, P., Gao, L., Ismagulova, T., Pilatova, J., Moudrikova, S., Gorelova, O., Solovchenko, A., Nedbal, L., Salih, A., 2020. Guanine, a high-capacity and rapid-turnover nitrogen reserve in microalgal cells. Proc. Natl. Acad. Sci. U. S. A. 117, 32722–32730.
Moreno, H., Archetti, L., Gibbin, E., Grandchamp, A.E., Frechin, M., 2021. Artificial intelligence-powered automated holotomographic microscopy enables label-free quantitative biology. Microscopy Today 29, 24–32.
Moudrikova, S., Ivanov, I.N., Vitova, M., Nedbal, L., Zachleder, V., Mojzes, P., Bisova, K., 2021. Comparing biochemical and Raman microscopy analyses of starch, lipids, polyphosphate, and guanine pools during the cell cycle of Desmodesmus quadricauda. Cell 10, 10010062.
Nemecek, D., Stepanek, J., Thomas Jr., G.J., 2013. Raman spectroscopy of proteins and nucleoproteins. Curr. Protoc. Protein Sci. 71. 17.8.1–17.8.52.
Nichols, S.L., Nilsson, E.M., Brown-Harding, H., LaConte, L.E.W., Acker, J., Borodavka, A., McDonald Esstman, S., 2023. Flexibility of the rotavirus NSP2 C-terminal region supports factory formation via liquid-liquid phase separation. J. Virol. e0003923.
Papa, G., Borodavka, A., Desselberger, U., 2021. Viroplasms: assembly and functions of rotavirus replication factories. Viruses 13, 1349.
Pasulka, A.L., Thamatrakoln, K., Kopf, S.H., Guan, Y., Poulos, B., Moradian, A., Sweredoski, M.J., Hess, S., Sullivan, M.B., Bidle, K.D., Orphan, V.J., 2018. Interrogating marine virus-host interactions and elemental transfer with BONCAT and nanoSIMS-based methods. Environ. Microbiol. 20, 671–692.
Rahman, S.K., Ampah, K.K., Roy, P., 2022. Role of NS2 specific RNA binding and phosphorylation in liquid-liquid phase separation and virus assembly. Nucleic Acids Res. 50, 11273–11284.
Roth, A.N., Aravamudhan, P., Fernandez de Castro, I., Tenorio, R., Risco, C., Dermody, T.S., 2021. Ins and outs of Reovirus: vesicular trafficking in viral entry and egress. Trends Microbiol. 29, 363–375.
Roy, P., 2020. Bluetongue virus assembly and exit pathways. Adv. Virus Res. 108, 249–273.
Rueden, C.T., Schindelin, J., Hiner, M.C., DeZonia, B.E., Walter, A.E., Arena, E.T., Eliceiri, K.W., 2017. ImageJ2: ImageJ for the next generation of scientific image data. BMC Bioinform 18, 529.
Sachse, M., Fernandez de Castro, I., Tenorio, R., Risco, C., 2019. The viral replication organelles within cells studied by electron microscopy. Adv. Virus Res. 105, 1–33.
Sandoz, P.A., Tremblay, C., van der Goot, F.G., Frechin, M., 2019. Image-based analysis of living mammalian cells using label-free 3D refractive index maps reveals new organelle dynamics and dry mass flux. PLoS Biol. 17, e3000553.
Shipp, D.W., Sinjab, F., Notingher, I., 2017. Raman spectroscopy: techniques and applications in the life sciences. Adv. Opt. Photonics. 9, 315–428.
Simoni, I.C., Bittencourt Fernandes, M.J., Marconi Custódio, R., Noronha Madeira, A.M.B., Weis Arns, C., 1999. Susceptibility of cell lines to avian viruses. Rev. Argent. Microbiol. 30, 373–376.
Strauss, S., Acker, J., Papa, G., Desiro, D., Schueder, F., Borodavka, A., Jungmann, R., 2023. Principles of RNA recruitment to viral ribonucleoprotein condensates in a segmented dsRNA virus. Elife 12, e68670.

Sung, P.Y., Vaughan, R., Rahman, S.K., Yi, G., Kerviel, A., Kao, C.C., Roy, P., 2019. The interaction of bluetongue virus VP6 and genomic RNA is essential for genome packaging. J. Virol. 93, e02023–18.

Taylor, N.O., Wei, M.T., Stone, H.A., Brangwynne, C.P., 2019. Quantifying dynamics in phase-separated condensates using fluorescence recovery after Photobleaching. Biophys. J. 117, 1285–1300.

Tenorio, R., Fernandez de Castro, I., Knowlton, J.J., Zamora, P.F., Lee, C.H., Mainou, B.A., Dermody, T.S., Risco, C., 2018. Reovirus sigmaNS and muNS proteins remodel the endoplasmic reticulum to build replication neo-organelles. MBio 9, e02023–18.

Tenorio, R., Fernandez de Castro, I., Knowlton, J.J., Zamora, P.F., Sutherland, D.M., Risco, C., Dermody, T.S., 2019. Function, architecture, and biogenesis of Reovirus replication Neoorganelles. Viruses 11, 288.

Touris-Otero, F., Cortez-San Martin, M., Martinez-Costas, J., Benavente, J., 2004. Avian reovirus morphogenesis occurs within viral factories and begins with the selective recruitment of sigmaNS and lambdaA to microNS inclusions. J. Mol. Biol. 341, 361–374.

Touris-Otero, F., Martinez-Costas, J., Vakharia, V.N., Benavente, J., 2004. Avian reovirus nonstructural protein microNS forms viroplasm-like inclusions and recruits protein sigmaNS to these structures. Virology 319, 94–106.

Tuma, R., 2005. Raman spectroscopy of proteins: from peptides to large assemblies. J. Raman Spectrosc. 36, 307–319.

Tuma, R., Bamford, J.H., Bamford, D.H., Thomas Jr., G.J., 1996. Structure, interactions and dynamics of PRD1 virus II. Organization of the viral membrane and DNA. J. Mol. Biol. 257, 102–115.

Tuma, R., Prevelige Jr., P.E., Thomas Jr., G.J., 1998. Mechanism of capsid maturation in a double-stranded DNA virus. Proc. Natl. Acad. Sci. U. S. A. 95, 9885–9890.

Tuma, R., Thomas Jr., G.J., 1997. Mechanisms of virus assembly probed by Raman spectroscopy: the icosahedral bacteriophage P22. Biophys. Chem. 68, 17–31.

Waldo, G.S., Standish, B.M., Berendzen, J., Terwilliger, T.C., 1999. Rapid protein-folding assay using green fluorescent protein. Nat. Biotechnol. 17, 691–695.

Walin, L., Tuma, R., Thomas Jr., G.J., Bamford, D.H., 1994. Purification of viruses and macromolecular assemblies for structural investigations using a novel ion exchange method. Virology 201, 1–7.

Walker, E.R., Friedman, M.H., Olson, N.O., 1972. Electron microscopic study of an avian reovirus that causes arthritis. J. Ultrastruct. Res. 41, 67–79.

Wei, M.T., Elbaum-Garfinkle, S., Holehouse, A.S., Chen, C.C., Feric, M., Arnold, C.B., Priestley, R.D., Pappu, R.V., Brangwynne, C.P., 2017. Phase behaviour of disordered proteins underlying low density and high permeability of liquid organelles. Nat. Chem. 9, 1118–1125.

Wiercigroch, E., Szafraniec, E., Czamara, K., Pacia, M.Z., Majzner, K., Kochan, K., Kaczor, A., Baranska, M., Malek, K., 2017. Raman and infrared spectroscopy of carbohydrates: a review. Spectrochim. Acta A Mol. Biomol. Spectrosc. 185, 317–335.

Wu, H., Volponi, J.V., Oliver, A.E., Parikh, A.N., Simmons, B.A., Singh, S., 2011. In vivo lipidomics using single-cell Raman spectroscopy. Proc. Natl. Acad. Sci. U. S. A. 108, 3809–3814.

Yakubovskaya, E., Zaliznyak, T., Martinez, J.M., Taylor, G.T., 2021. Raman microspectroscopy Goes viral: infection dynamics in the cosmopolitan microalga, *Emiliania huxleyi*. Front Microbiol 12, 686287.

Zhang, X., Tang, J., Walker, S.B., O'Hara, D., Nibert, M.L., Duncan, R., Baker, T.S., 2005. Structure of avian orthoreovirus virion by electron cryomicroscopy and image reconstruction. Virology 343, 25–35.

Zhu, X., Xu, T., Peng, C., Wu, S., 2021. Advances in MALDI mass spectrometry imaging single cell and tissues. Front. Chem. 9, 782432.

Zwicker, D., Decker, M., Jaensch, S., Hyman, A.A., Julicher, F., 2014. Centrosomes are autocatalytic droplets of pericentriolar material organized by centrioles. Proc. Natl. Acad. Sci. U. S. A. 111. E2636–45.